INTERNATIONAL ATOMIC ENERGY AGENCY
UNITED NATIONS EDUCATIONAL, SCIENTIFIC AND CULTURAL ORGANIZATION

INTERNATIONAL CENTRE FOR THEORETICAL PHYSICS
34100 TRIESTE (ITALY) - P.O.B. 586 - MIRAMARE - STRADA COSTIERA 11 - TELEPHONES: 224281/2/3/4/5/6
CABLE: CENTRATOM - TELEX 460392 I

SPRING COLLEGE ON AMORPHOUS SOLIDS
AND THE LIQUID STATE

14 April - 18 June 1982

RECENT FUNDAMENTAL AND APPLIED DEVELOPMENTS IN THE AMORPHOUS SILICON FIELD

W.E. SPEAR

Carnegie Laboratory of Physics
University of Dundee
Dundee DD1 4HN
Scotland, UK

Recent Fundamental and Applied Developments in the Amorphous Silicon Field.

W.E. Spear

Carnegie Laboratory of Physics,
The University, DUNDEE DD1 4HN,
Scotland, U.K.

1. Introduction

The following notes should provide a fairly detailed background to my lectures at the 1982 Spring College on 'Amorphous Solids and the Liquid State'. In particular most of the diagrams are identical to the slides and transparencies that will be discussed during the lectures and this should help students in following the course. The text is partly based on a recent review article by Spear and LeComber and includes many relevant references to current work in the amorphous silicon (a-si) field.

The lectures are concerned specifically with the properties of a-Si prepared in a radio-frequency (r.f.) glow discharge by decomposing silane which may contain small amounts of doping gases. The subject has now reached an important, perhaps even critical stage: the fundamental developments during the 1970s in the field of glow discharge Si have established the considerable applied potential of this material and we are now beginning to see a rapid growth of applied developments, in some cases already on an industrial scale. It is therefore essential that the course should deal with both these aspects and should attempt to relate the fundamental insight into the material properties with the applied possibilities which have led to the present world-wide activity in the a-Si field.

The lectures are built around two aspects of fundamental importance to the present developments, both of which arose out of the work of the Dundee group. The first concerns the density of states in the mobility gap of glow discharge Si, studied by the field effect and more recently by other techniques. Already in 1972 our early field effect experiments led to the realisation that a-Si possessed a remarkably low level of gap states; this is probably the most important single factor which makes a-Si into an electronically viable material for fundamental and applied work. A direct result on the applied side has been the a-Si field effect transistor discussed in Section 5, which could find application as a switching element in large area addressable displays and in other devices.

The second crucial development was the discovery in 1975 that the electronic properties of the glow discharge material could be controlled very effectively by substitutional doping from the gas phase; again, this is closely related to the low gap state density of the material. The possibility of doping has opened up the rapidly growing field of a-junction devices, which will be discussed in Section 7 with particular reference to the materials aspect.

We shall begin with a subject common to all following lectures, namely the glow discharge technique itself. Deposition systems, on a laboratory and industrial scale, will be discussed, as well as some of the recent work on deposition rate and the silane plasma.

2. The Glow Discharge Technique.

With the limited information presently available on the processes taking place in the glow discharge plasma, it is not surprising that the techniques for the preparation of a-Si from a silane glow discharge were developed largely on an empirical basis. Accordingly, we shall begin with a discussion of reactors, techniques and deposition conditions which have been found to produce electronically viable a-Si specimens. In Sect.2.4 some of the recent work aimed at a more detailed understanding of the plasma will be summarised.

2.1 Radio Frequency Deposition Systems.

Glow discharge preparation units can be divided into two groups, depending on the method of coupling the radio frequency (r.f.) excitation into the plasma. The first glow discharge deposition of a-Si was carried out in an inductively coupled system by STERLING and his collaborators [1][2] at the S.T.L. Laboratories. The same approach was adopted in the early work of the Dundee group on the electronic properties of the material [3][4] and inductively coupled reactors are still used as a convenient method for depositing small area specimens. Figure 1 illustrates the method. The gas G, (silane or an appropriate gas mixture), is passed through a fused silica reaction tube Q, between 5 and 10 cm in diameter. The pressure lies in the range from 0.1 to 1 torr at gas flow rates between 0.1 and 10 cubic centimetres per minute at S.T.P. A rotary pump RP, sometimes fitted with a Roots blower, maintains the gas flow through the system. The substrate S is held on the heated pedestal H, which is immersed in the lower part of the glow discharge plasma P. The latter is excited by an external coupling coil connected to an r.f. generator, normally operated at a frequency of 13.56 MHz.

It is important to note that the film grows in close contact with the plasma and that its electronic properties are critically dependent on the interactions taking place at the interface. In spite of the simplicity of the basic arrangement of Fig.1 the reproducibility and quality of the specimens can be maintained only by careful attention to all the parameters involved. Electronic properties as well as hydrogen content are also dependent on the dimensions of the system, presumably as a result of floating potentials on surrounding surfaces. In our experience the height of the r.f. coil above the substrate is a sensitive variable, as are the substrate temperature T_d and the r.f. power level. It has generally been found (see Sect.3) that for the lowest densities of gap states T_d-values between 250°C and 330°C are required, together with a low level of r.f. power (1-10W), just sufficient to maintain a weak glow discharge.

The second type of deposition system employs capacitative coupling. Figure 2 shows a versatile unit of this kind designed by KNIGHTS [5][6]. An obvious advantage over the inductive system lies in the relative ease with which the parallel plate geometry can be scaled up for the uniform deposition of larger area specimens (see Sect.2.2). It can be seen that the upper electrode, holding the substrates, can either be connected to r.f. ground potential (i.e. that of the surrounding metal box) or to the 'hot' r.f. electrode via the matching network and a coupling capacitor. In the latter case the substrate surface will acquire a steady negative bias which, as shown by KNIGHTS [6], can influence the material properties. Typical values of parameters such as pressure, flow rate, substrate temperature and r.f. power mentioned above apply equally well to the capacitative system.

Figure 3 is a schematic diagram of a system that has been used in the Dundee laboratories during the last few years. The main aims of the design have been to reduce the contamination problem and to achieve optimum versatility,

particularly for the deposition of multi-layer specimens. The stainless steel specimen holder S and its electrically insulated heater H are mounted vertically to reduce the deposition of small particles which are difficult to eliminate completely from a plasma system. S is held in a demountable quartz enclosure Q and the r.f. field is applied between the external electrodes E which are electrically connected together and adjusted parallel to the surface of S. The whole of the specimen holder assembly is insulated from ground and can easily be withdrawn from the apparatus for substrate loading. Two thermocouples are incorporated to monitor the temperature of the holder and of the substrate surface respectively. Rotatable 'flaps' F have been fitted which can be operated during a deposition run to shade certain regions of the substrate. Such a facility has proved to be very useful in the development of junctions and other multi-layer devices. An obvious advantage of the vertical arrangement over that shown in Fig.2, is that both sides of the holder S can be used; in our largest unit this gives a total useable area of 300cm^2.

R.F. generators, operating at 5.0, 13.56 and 40.68 MHz, can be connected through a power controller PC and a matching network MN between the external plates E and the holder assembly S. The gas handling system is made entirely from stainless steel and consists of the five channels indicated in Fig.3, all connected to the mixing chamber M. Each channel is fitted with a mass flowmeter and a piezoelectric valve for electronic flow and ratio-control. In addition several 1-litre reservoirs such as R are connected to M, enabling the operator to flow pre-mixed gases through the system. Nitrogen flushing lines, essential for safe operation, are provided at several parts of the apparatus.

The whole system is normally kept under high vacuum produced by the 3000 litre s^{-1} cryopump CP. We believe that this helps considerably in reducing cross-contamination from gases that have been used in previous runs. During a deposition run CP is shut off and the gas flow is maintained by the rotary pump RP.

The tubular furnace TF mounted in front of the pump decomposes the hydrides, which reduces contamination of the pump oil and adds to the safety of the system. The mass spectrometer MS is a useful part of the unit, allowing examination of a gas sample before deposition. Finally, to comply with safety regulations, the whole apparatus, including the gas supplies, are kept in a continuously ventilated enclosure which can be completely isolated from the laboratory.

2.2 Large Scale Deposition.

The reactors described in the previous section are useful in the research or development laboratory for preparing a limited batch of specimens, but they are hardly suitable for industrial production on a larger scale. The rapid growth during the last few years in the field of a-Si photovoltaic devices has stimulated interest in the industrialisation of the glow discharge technique. At the 1981 Grenoble Conference, KUWANO and OHNISHI [7] of the Sanyo laboratories described the design of what is probably the first industrial plant for the production of a-Si devices.

As shown schematically in Fig.4, the system consists of five separate vacuum chambers, connected by vacuum locks. Trays loaded with substrates are placed into the first chamber on the right and then pass in a continuous process through the three central chambers in which boron doped, undoped and phosphorus doped layers are deposited to form the p-i-n photovoltaic junction. The main advantage of separating these stages is that problems arising from dopant contamination are completely avoided. The latter can partly be overcome in the smaller systems described earlier, but would seriously affect reproducibility in a continuous industrial process. Another important point is that the central deposition chambers are not exposed to air, except for occasional maintenance.

In spite of the greater cost and complexity of the Sanyo system over possible single chamber designs in which the gases are cycled, its advantages are considerable and it is likely that future industrial developments will follow along similar lines.

2.3 The Deposition Rate and the Use of Higher Silanes.

Experience has shown that high quality a-Si films have to be prepared in the silane glow discharge at deposition rates of less than about 3Å s^{-1} and with the minimum r.f. power. Under these conditions ion and electron energies in the plasma remain sufficiently low to reduce defect formation at the growing surface to an acceptable level. The present limitation imposed by the deposition rate is not too serious in laboratory work involving specimens a fraction of a micron in thickness. However, for thicker films such as those discussed in Sect.7.4, deposition times tend to become unacceptably long.

Can this limitation be overcome? Recently SCOTT et al [8][9] have investigated the deposition and electronic properties of glow discharge a-Si specimens produced from di-silane (Si_2H_6) and tri-silane (Si_3H_8), both of which form less stable molecules than the mono-silane used in the previous work. The encouraging result was that with a low r.f. power (2W in an inductively coupled system) the deposition rate from the higher silanes was more than 20 times larger than that obtainable from SiH_4. Moreover, films up to 20μm thick could be deposited, presumably because of reduced film-substrate strain.

According to the information published so far, the electrical and photoconductive properties of films rapidly deposited from Si_2H_6 appear to be substantially the same as those obtained in specimens from SiH_4 but produced at a much smaller rate.

In view of the comparatively high cost of commercially available di-silane, it is tempting to explore the possibility of producing higher silanes directly within the present experimental set-up. Figure 5 shows the method adopted by OGAWA et al [10] in their recent study of enhanced deposition rate. Higher silanes are formed by circulating mono-silane through an ozoniser tube connected to a 6kV transformer and condensed into a cold trap. Remaining gaseous products, such as hydrogen or SiH_4, are then pumped away. The mixture of higher silanes is introduced into the glow discharge by allowing the trap to warm up. OGAWA et al deposited specimens in this apparatus at a rate exceeding 60Å s^{-1} and a substrate temperature of 350°C. Measurements showed that the optical gap, the activation energy and the dark-and photo-conductivities are substantially the same as those obtained from mono-silane at appreciably lower deposition rates.

The recent developments described in this section are most encouraging and, provided the performance of a-Si devices can be maintained at the higher deposition rates, could prove to be of considerable importance in large scale applications of a-Si.

2.4 Recent Studies of the Silane Plasma.

In spite of the widespread use of the glow discharge techniques described in the previous sections, the reactions taking place in the silane plasma, and particularly at the plasma-substrate interface, are still largely unknown. In the following we shall discuss briefly the nature of the plasma and summarise some of the present work aimed at a closer understanding of the processes involved in the deposition of a-Si.

The weak glow discharge employed here produces a dilute plasma state which comprises a wide variety of species: electrons, ions, excited neutrals

(both free radicals and gas molecules), and photons. All these participate in the interactions to varying degrees. The electrons possess average energies between 0.5 and 5eV, which means that their effective temperature is 10 to 100 times that of the gas ($\propto T_d$). Electron densities are about 10^{10} cm^{-3}, approximately equal to that of the positive ions. The r.f. glow discharge is maintained by inelastic electron collisions, which in the case of the silane plasma lead to reactive neutral species such as SiH, SiH_2, SiH_3, Si_2H_6, H, H_2 and ionised species SiH^+, SiH_2^+, SiH_3^+ etc. More detailed information on the silane glow discharge is given in the review article by GRIFFITH [11], who also considers likely electron impact processes which lead to the above species.

Figure 6 is an example of a typical optical emission spectrum from a pure silane glow discharge plasma obtained by MATSUDA and TANAKA [12]. The r.f. power was 20W and, by means of an optical fibre system, the emission from a region close to the substrate could be recorded. The spectrum shows primary neutral species such as SiH, H_2 and the H_α and H_β lines of the BALMER series. The prominent SiH band contributes to the violet appearance of the silane glow discharge. Species such as SiH_2 and SiH_3 have no known emission spectrum.

3. Field Effect and the Density of States in a-Si.

The work on a-Si during the last decade has demonstrated the critical dependence of the electronic properties of this material on the density and distribution of localised states. The independent measurement of the distribution function $g(\varepsilon)$, defined as the number of states per unit volume in unit energy interval, is therefore of considerable importance. In fact the $g(\varepsilon)$ measurements on a-Si in the early 1970s, using the field effect technique [13][14][15][16], provided a wealth of information on the effect of preparation technique and deposition conditions on $g(\varepsilon)$; this contributed greatly to the subsequent development of the subject. In spite of the difficulties of the experiment and particularly the analysis of the data, the field effect experiment still appears to be the most promising approach to the determination of $g(\varepsilon)$. Recently, for example, it has been used to study the effect of hydrogen evolution and of illumination on the creation of defects in a-Si. Furthermore, the field effect experiments on a-Si have led to the development of the thin-film transistor which forms the subject of section 5.

The aim of this section is to review the principle and analysis of the field effect experiment, discuss the calculated density of state distribution and finally compare these with the results from independent measurements.

3.1 Principle and Experimental Details of the Field Effect Experiment.

In the experiment, the localised state distribution is investigated by displacing it with respect to the Fermi level ε_f. This is done by means of an external electric field, applied in a direction normal to the surface of the film to be studied. The energy range moving past ε_f as the field is increased, can be calculated from the measured changes in the specimen conductivity. The major experimental problem consists of applying as large a field as possible without any significant leakage current into the specimen. Figure 7 shows two arrangements that have been widely used [14] [15]. In (a) the a-Si film is deposited directly onto a thin ($\approx 170\mu m$) quartz substrate Q, which also acts as the dielectric for applying the external field. The other surface contains the narrow gate electrode G which is carefully aligned with the gap between the source and drain electrodes, S and D, deposited on the

free surface of the a-Si film. The measurement consists of applying a relatively small constant voltage V_{SD} between the source-drain contacts and recording the specimen current I_D as voltages V_G, of up to 10-15 kV, are applied between the gate electrode and the free surface of the a-Si, which will remain essentially at earth potential. Measurements are made for both positive and negative V_G.

The main disadvantage of using the quartz substrate as the dielectric is the necessity for large gate voltages. This can be overcome by the thin-film insulator shown in Fig.7(b) [14][15]. A film ($\lesssim$ 1μm) of amorphous silicon nitride (a-Si-N) is deposited by the glow discharge process onto a substrate which carries the evaporated gate electrode G. The a-Si is deposited directly onto this Si-N film and source and drain electrodes are then evaporated as before. In this way much higher fields can be applied with comparatively low voltages, significantly extending the range of measurements.

In addition to providing important information on the localised state density, the field effect experiment also gives the sign of the majority carriers in the amorphous sample.

The magnitude of the changes in I_D are critically dependent on the magnitude of $g(\varepsilon)$ in the material, with a low $g(\varepsilon)$ giving the largest changes. Evidently, useful information about the general features of $g(\varepsilon)$ can be obtained directly from the experimental data.

The field effect experiment can, however, suffer from one major limitation which in extreme cases could invalidate the above general conclusions. Underlying the interpretation of the data is the basic assumption that the localised states which screen the field are representative of a volume distribution rather than interface states. Little is known about surface states on amorphous semiconductors and we have always taken the view that the only reasonable way to test the above assumption is to assess critically the deduced distribution in the light of measurements of other volume properties [17]. We shall return to this point in Sect.3.5.

3.2 Field Effect Results on a-Si.

3.2.1 Glow Discharge Samples

Figure 8 shows a number of field effect curves for glow discharge Si specimens deposited at T_d = 250°C [14]. The results in Fig.8(a) were obtained using Si-N as the dielectric, those in Fig.8(b) with quartz. The most obvious feature is the large rise in I_D when V_G increases in the positive direction. This leads to the conclusion that the overall density of states is relatively small and also that the current in these specimens is carried predominantly by electrons. In contrast, samples produced at T_d < 80°C invariably indicated p-type conduction as shown in Fig.9 (a) for a specimen deposited at T_d = 40°C onto a Si-N dielectric [14]. In addition, the overall change in I_D is minute compared to that in high T_d samples, indicating a significantly larger density of states.

Figures 9 (b) and (c) illustrate the effect of annealing the low T_d specimen [14]. After the first stage of annealing at T_A = 140°C, (Fig. 9(b)) the specimen has undoubtedly been converted to predominant electron conduction and its state density at the Fermi level has been reduced. Further annealing at T_A = 210°C (Fig. 9 (c)) continues this process very effectively, as is apparent from the large increase in the range of I_D which now extends over three orders of magnitude.

3.2.2 Evaporated and Sputtered Samples.

In general, field effect experiments on evaporated specimens either gave no observable change in I_D, or a very small p-type response,

even at the highest gate voltages used, unless the samples were subsequently annealed or were evaporated in a poor vacuum [14]. Similar results have also been obtained on samples prepared by sputtering. However, it is possible to significantly decrease $g(\epsilon)$ of this material by sputtering in a gas mixture containing hydrogen. [18]

The experiments support the suggestion, based on electrical conductivity, drift mobility and optical data [4][14], that evaporated and sputtered films have a much higher localised state density than glow discharge specimens, leading to significant differences in the optical and electrical properties.

In the next section we summarise the approaches that have been used to calculate the density of state distribution from the experimental field effect data.

3.3 Analysis of the Field Effect Results.

The calculation of $g(\epsilon)$ from the experimental field effect data is a complex problem which has attracted quite a lot of attention during the last few years. All the methods of analysis, discussed in the following, involve two common assumptions; first, the semiconductor is homogeneous and secondly, the effect of interface states can be neglected except that they may, if present, produce band bending at zero gate voltage. The validity of these assumptions will be discussed in Sec.3.5.

We begin by considering the step-by-step method of analysis in which $g(\epsilon)$ is progressively deduced from the observed current I_D as V_G is increased in equal steps ΔV_G. This approach, developed by Spear and Le Comber for the analysis of the early field effect results on a-Si [13], involved in its original form three simplifying assumptions. The first of these was concerned with the potential profile $V(x)$ in the semiconductor, which was assumed to have the

form of a Schottky barrier or an exponential barrier; this neglected the effect of the localised state distribution on the shape of the barrier (c.f. Sect.7.1). Poisson's equation can then be solved to relate the band bending $u_s kT$ at the surface, (see Fig.7(c)), with the spatial extent λ of the barrier. By integrating the current contributions throughout the sample thickness it is possible, at any step in the experiment, to determine u_s and λ from the measured I_D. Finally, the total excess charge eN_s induced in the semiconductor at the given V_G is required. This can readily be calculated from the known capacitance between gate and semiconductor.

The next problem consists of deducing $g(\epsilon)$ from eN_s, u_s and λ as the distribution is moved past ϵ_f by the ΔV_G steps. A simple solution, adopted in the earlier work, rested on the assumption that the induced charge carriers occupied previously empty states within $u_s kT$ of ϵ_f over a distance λ. This implied (i) zero temperature statistics and (ii) abrupt band bending, inconsistent with the above form of $V(x)$. In a subsequent publication [16] these two approximations were removed; the simple procedure was initially used to obtain $g(\epsilon)$ to first approximation. Based on this solution, the form of the field effect response curve was calculated by numerical methods. Small changes in $g(\epsilon)$ were then made until agreement between predicted and experimental curves was achieved. The work showed that the main quantitative change produced by this refinement was to increase $g(\epsilon)$ by a factor of between two and three.

Even the refined step-by-step method still relies on an assumed form of $V(x)$. This limitation was removed by GOODMAN and FRITZSCHE [19] who started the analysis with a trial solution for $g(\epsilon)$, and obtained a numerical solution of Poisson's equation with a self-consistent $V(x)$. $g(\epsilon)$ (and $V(x)$) were then modified until the predicted and experimental field effect characteristics agreed. Although more exact than the step-by-step procedure, this

approach involves considerable computing time and produces results that differ from the simpler method by less than a factor of two (see for example Fig.3 of ref.[19]). Subsequently, it has been pointed out and demonstrated by a number of authors [20][21][22], that the Goodman-Fritzsche method can be simplified by a change of the independent variable in Poisson's equation, with a significant reduction in computing time.

A basically different approach was followed by GRÜNEWALD et al [23] who published a method for calculating the induced space charge density $\varrho(v)$ directly from the experimental data. The density of states has then to be found by deconvoluting

$$\varrho(v) = e \int_{-\infty}^{+\infty} g(\varepsilon) \, [f(\varepsilon - eV) - f(\varepsilon)] \, d\varepsilon \qquad \text{——— (3)}$$

where f( ) is the Fermi distribution function.

We mentioned earlier that all the methods of analysis assume that the only effect of interface states might be to produce some band bending at zero gate voltage. The calculated values of $g(\varepsilon)$, at least near ε_f, are sensitive (within a factor of 2 to 3) to the choice of the flat-band position on the V_G-axis. This value can not be determined unambiguously from field effect data at a single temperature. However, it can be deduced, at least in principle, from experiments at different temperatures [21][22].

In summary the determination of $g(\varepsilon)$ from field effect data is a complex problem that can only be solved either by making a number of simplifying assumptions, as in the step-by-step method, or by numerical techniques involving a trial solution for $g(\varepsilon)$ which is then adjusted until agreement between the calculated and experimental field effect conductance is obtained. Generally, these two approaches lead to similar results, although small features in $g(\varepsilon)$, sometimes found by the former, are not always uniquely determined by the latter.

Finally, before discussing some of the calculated $g(\varepsilon)$ results, it is worth noting that the neglect of interface states and the difficulties associated with the choice of the flat-band voltage, probably introduce larger uncertainties in $g(\varepsilon)$ than those produced by the different methods of analysis!

3.4 Discussion of Calculated $g(\varepsilon)$ Data.

Figure 10 shows the calculated density of states [14][15] for a number of glow discharge a-Si films, deposited at the indicated values of T_d. $g(\varepsilon)$ is plotted against the energy normalised to the electron mobility edge at ε_c; the position of the Fermi level for each sample is indicated by the arrow. The full-line portions were calculated from the experimental data and the dotted parts were based on an extrapolation procedure. The results range from ε_A, situated about 0.2eV below ε_c, to almost ε_y which was previously associated with hole hopping transport [4]. The curves in Fig.10 lead to a number of important conclusions [14]: (i) the overall level of the localised state density, at least between ε_y and ε_A, is a strong function of the deposition temperature; (ii) a minimum in $g(\varepsilon)$ exists close to the centre of the gap; (iii) $g(\varepsilon)$ increases as $\varepsilon_c - \varepsilon$ approaches ε_y which, in agreement with conductivity and photoconductivity results [24], is situated at $\varepsilon_c - \varepsilon_y \simeq 1.2$eV; (iv) between ε_A and ε_c there is a rapid increase in $g(\varepsilon)$, which has been identified with a range of electron tail states, about 0.2eV wide. Sample 1 in Fig.10, deposited at T_d = 300°C, is representative of the high-T_d specimens. It is clearly n-type and the density of states near the centre of the gap is remarkably low, $\lesssim 10^{17}\,cm^{-3}eV^{-1}$. As the deposition temperature is lowered, the general level of $g(\varepsilon)$ increases and ε_f moves closer towards the centre of the gap. Eventually for specimens deposited at T_d < 350K (sample 6a for example), the Fermi level has moved so close to ε_y, that the dominant conduction mechanism is now by holes hopping at this energy.

Substitutional doping in a-Si (see Sect.3) has made it possible to shift ε_f throughout most of the mobility gap, so that $g(\varepsilon)$ can be determined for high-T_d specimens over a larger energy range than covered in Fig. 10. Figure 11 includes the results for a number of undoped and comparatively lightly doped samples. The $g(\varepsilon)$ data in the centre of the gap were determined as before on undoped material. The Fermi level positions denoted by ε_{f6}, ε_{f5} and ε_{f4} refer to specimens doped with an increasing level of P, and the results give more information on $g(\varepsilon)$ in the region of the electron tail states. On the other hand, light B-doping moves ε_f towards the valance band and extends the $g(\varepsilon)$ range to energies of over 1.2eV below ε_c. It must, however, be emphasised that the results obtained in Fig.11 with the doped specimens give no information on the effect of doping on $g(\varepsilon)$ in the central region of the gap. It is possible that moderate or heavy doping can produce an increase of $g(\varepsilon)$ in this energy range.

3.5 Comparison of the Deduced $g(\varepsilon)$ with other Measurements.

The calculation of $g(\varepsilon)$ from the field effect experiment rests on the basic assumptions that the effect is representative of a homogeneous bulk property of the a-Si and is not dominated by interface states at the gate insulator. In our view the best test of this assumption is to compare the $g(\varepsilon)$ data with independent measurements of the bulk properties [13][14][15][16]. The evidence from extensive electrical and optical measurements has been reviewed in some detail previously [17] and we shall therefore refer here only briefly to this work.

Measurements of electrical conductivity [4], optical absorption [24], photoconductivity [25] and drift mobility [3][4] all provide independent support for the general features in $g(\varepsilon)$ shown in Figs. 10 and 11. Furthermore the effect of doping, either from the gas phase[26][27] or by ion implantation[28][29], also provides evidence for the broad minimum in $g(\varepsilon)$ near the centre of the gap and the rise in $g(\varepsilon)$ near ε_A and ε_y. It can therefore be concluded that, in spite of the difficulties associated with the field effect and its analysis, it does provide us in a-Si with a density of states distribution that is consistent with independent measurements of bulk properties.

The technique of deep level transient spectroscopy (DLTS) has recently been applied to a-Si [30][31][32] and the results were used to deduce the density of localised states. As with the field effect, certain assumptions had to be made in order to calculate both the magnitude of $g(\varepsilon)$ and the energy scale. However, the above authors stress as a major advantage of DLTS over the field effect technique the fact that it leads to a true bulk density of states, unaffected by interface or surface states. In their original paper COHEN et al [30] deduced $g(\varepsilon)$ values for two samples in which the conductivity was considerably higher than normal, although these films were not intentionally doped. Values of $g(\varepsilon)$ as low as $2 \times 10^{14} cm^{-3} eV^{-1}$ were reported, but these values were increased in a subsequent publication [32], and are represented in Fig.12 by the line marked DLTS. Comparison with a typical field effect $g(\varepsilon)$ denoted by F.E. in Fig. 12, shows that as well as giving significantly lower $g(\varepsilon)$ values, the DLTS technique also suggests a widely different distribution with a deep minimum in $g(\varepsilon)$, 0.4 to 0.5 eV below ε_c.

The analysis of space charge limited current flow in a-Si provides an independent alternative approach to the $g(\varepsilon)$ problem. It is particularly relevant in the present controversy, because there is no doubt that the space charge limited current (SCLC) is determined by the volume distribution of localised states. Extensive work on SCLCs in a-Si has recently been

carried out by DEN BOER [33] and by MACKENZIE et al [34] in our laboratory. A typical current-voltage characteristic for the highly injecting n^+-i-n^+ structures used is shown in Fig.20 (Sect.7.2). With relatively minor approximations these measurements lead to the bulk $g(\varepsilon)$ values shown by the points and the dashed line in Fig.12 [34]. The full line marked D.B. represents the average of DEN BOER'S [33] results. Clearly, there is satisfactory agreement between the results obtained in the two laboratories on different specimens. Furthermore the values of $g(\varepsilon)$ in the range investigated lie between 2×10^{16} and $10^{17} cm^{-3} eV^{-1}$ and follow the shape of the field effect data rather than that from the DLTS studies. On this basis it would appear that the DLTS technique considerably underestimates the density of states in a-Si. In view of the uncertainty by a factor of two to three in the precise magnitude of $g(\varepsilon)$ from field effect and the somewhat smaller uncertainty in the data from SCLC, it also appears from Fig.12 that interface states can have relatively little effect on the field effect results.

4. The Transport Properties of Glow Discharge a-Si.

As the transport properties and mechanisms in a-semiconductors have been dealt with in previous lecture courses we shall confine ourselves in this section to a brief summary of these properties for a-Si prepared by the glow discharge process.

4.1 Conductivity and Drift Mobility

The electronic transport in undoped a-Si has been studied extensively during the early 1970s by the Dundee group. In particular the combination of conductivity and drift mobility experiments has led to important conclusions which have stood the test of time. As shown in the previous section, the density of state distribution depends critically on preparation conditions and the same applied to the transport properties. Unless otherwise stated, the following results refer to specimens deposited under optimised plasma conditions (see sect.2.1) and at a deposition temperature of $T_D \approx 300°C$.

(i) The temperature dependence of conductivity and drift mobility [3][4] shows that at $T \gtrsim 250K$ electrons propogate in the extended electron states at ε_c with a mobility μ_c between 1 and $10 cm^2 V^{-1} s^{-1}$. Below that temperature, phonon-assisted hopping through the localised tail state distribution near ε_A (see Fig.11) begins to predominate. The hopping mobility is about $10^{-2} cm^2 V^{-1} s^{-1}$.

(ii) The observed conductivity activation energy for undoped specimens is 0.70 - 0.75eV, which represents $\varepsilon_c - \varepsilon_f$ extrapolated to T = 0. As discussed in the paper by Anderson and Spear [35] the Fermi level position is likely to be determined by the overlap of two distributions of states. Although the hole mobility μ_v in the extended states at ε_v is believed to be similar to μ_c,

holes contribute little to the observed thermal equilibrium conductivity in undoped specimens. The reason is the asymmetry of ϵ_f in the mobility gap which makes $\epsilon_f - \epsilon_v \approx 0.95$eV.

(iii) The measured drift mobility of excess electrons and holes is controlled by a multi-trapping process. During transit, excess electrons interact by trapping and thermal release with states near ϵ_A [3][4]; excess holes interact with states near the ϵ_y maximum [36] which makes the hole drift mobility about 1/100th of that of the electrons.

(iv) Decreasing T_D moves ϵ_f into the centre of the mobility gap; electron transport predominates up to $\epsilon_c - \epsilon_f \approx 0.85$eV. But in specimens prepared at $T_D \lesssim 80°C$, ϵ_f lies in the lower half of the mobility gap and the predominant transport mechanism is by hopping, probably in the region of ϵ_y [15].

(v) In phosphorus doped specimens, drift mobility experiments show that a fraction of the excess electrons propagate by hopping through the donor states [37][38]. From the dependence of the hopping mobility on the average donor separation it is deduced that the donor wave functions in a-Si extend about 22Å around the phosphorus donor.

4.2 Thermo-electric power

The thermo-electric power, S, is determined by the weighted average over the energy difference between ϵ_f and the various current paths through the energy spectrum. The sign of S gives unambiguous information on the predominant charge carrier. As shown by the extensive work at Marburg [39] and at Dundee [40][38], measurement of S provides an extremely sensitive and clear-cut method for the study of the electronic properties of a-Si and other a-semiconductors. It is of interest to compare

the value of $\epsilon_c - \epsilon_f$ deduced from thermo-electric power with that from conductivity measurements. Small differences (0.05-0.1eV) are observed at room temperature which disappear at higher T in carefully prepared specimens. The effect has been ascribed to long-range potential fluctuations [41] in the current path at ϵ_c.

4.3 Hall Effect.

Hall Effect measurements in a-materials are no longer the useful and interpretable approach to transport studies which they were in crystalline semiconductors. Nevertheless, the theory of the Hall Effect in non-crystalline solids, where long-range order is absent, provides interesting fundamental problems [42][43]. One of these is the double reversal in the sign of the Hall coefficient for n- and p-type a-Si, first demonstrated by the Dundee work [44][38]. It is significant that this effect disappears as soon as a very limited amount of long range order is established, as is clearly shown by the results described in section 8.3.

4.4 Photoconductivity

The high photoconductivity of glow discharge a-Si is of considerable fundamental and applied interest. Our early work on this subject was concerned with the spectral dependence and with the lifetime of photogenerated carriers as a function of deposition temperature [24][15]. A subsequent paper [25] dealt with the temperature dependence of photoconductivity, the recombination process and its relation to the density of state distribution. In a good undoped specimen the recombination lifetime of the photogenerated electrons approached 10^{-5}s. As shown in the more recent study of the effect of doping on photoconductivity [35], light phosphorus doping leads to a remark-

able sensitisation of the photoresponse. This occurs when $\epsilon_c - \epsilon_f$ is reduced to values below 0.6eV and ϵ_f moves through the 'tail' of positively charged states, filling these centres. The lifetime of the photo-electrons then increases to values above 10^{-4}s.

In summary, the most significant transport property of glow discharge Si discussed in this section is the existence of predominant extended state conduction at room temperature and below, a feature which is of course directly related to the low overall g(ε) that can be achieved.

5. The a-Si Field Effect Transistor and its Possible Applications.

The field effect experiments described in section 3 demonstrated that a-Si deposited by the glow discharge process has a remarkably low density of gap states, which is a basic requirement for most electronic applications. Another advantage of the glow discharge technique is that it can be used to deposit sequentially thin layers of different materials, simply by changing the gas composition. This procedure has found increasing use in the development of the a-Si field effect transistor (to be referred to as FET in the following), which forms the subject of this section. The possibility of this application was originally suggested by the field effect studies in the 1970s [13],[14],[15] which showed that large current changes could be obtained for moderate fields produced by the gate electrode.

In 1976 the Dundee group and colleagues at RSRE, Malvern, jointly proposed the use of a-Si field effect devices in the addressing of liquid crystal matrix displays as an alternative to the thin film CdSe transistors which had been developed by BRODY and co-workers [45]. They reasoned that an elemental covalently bonded material such as a-Si should have distinct advantages over the more complex II-VI compounds as far as ease of preparation,

reproducibility and stability are concerned. The design and characteristics of an a-Si insulated gate FET suitable for driving liquid crystal displays were published by LE COMBER et al [46], and experiments at RSRE showed that such a device could switch liquid crystal elements satisfactorily.

In the following we shall consider the design, characteristics and fabrication of a-Si FETs and discuss their possible applications in addressable liquid crystal displays, logic circuits and image sensors [47].

5.1 Design and Characteristics of Elementary Device.

The basic design of the a-Si FET element is shown schematically in the insert to Fig.13. It represents a direct development of the arrangement originally used in the field effect experiments described in Sect.3.1. A metal electrode, typically 50μm wide, is first evaporated onto a glass substrate to form the gate electrode. A thin insulating layer, 0.4μm or less, of amorphous silicon nitride (Si-N), is then deposited by the glow discharge technique to form the gate dielectric. This is followed by an a-Si layer, also a few tenths of a μm thick. The final step consists in depositing the required pattern of source and drain contacts on to the a-Si surface. It is an essential point for any future application of these devices that large area arrays can be produced reproduceably and cheaply. In this connection it is most important that conventional photolithographic techniques have been successfully applied to the fabrication of arrays of a-Si/Si-N FETS [48].

The dc performance of an elementary device with a 40μm channel length and a 500μm channel width, produced by photolithographic techniques, is illustrated by the transfer characteristics shown in Fig.13. The source-drain current I_D is plotted logarithmically against the gate voltage V_G for drain potentials of 2V, 10V, and 20V. It can be seen that with +15V on the gate, drain currents in excess of 1μA can be achieved for drain voltages as

low as 5V. In the off-condition, with $V_G = 0$, the current through the device drops below 10^{-11}A. The remarkable rise in I_D is caused by an electron accumulation layer formed at the Si/Si-N interface, which produces an efficient current path between the source and drain electrodes.

The radiation hardness of a-Si FETs could be significant in some applications. Preliminary results obtained with γ-radiation from Cobalt 60 indicate that doses up to 11 Mrads, the maximum used, have relatively little effect on the dc characteristics of the devices.[49].

5.2 Application - Addressable Liquid Crystal Displays.

Liquid crystal displays are potentially very attractive for large-area applications as they are low power devices and have good visibility in high ambient light conditions. However, the difficulty of multiplexing large arrays of such devices has so far limited their use. If a small non-linear device, such as an FET, is used to control each display element, much larger arrays could in principle be addressed. Liquid crystal devices typically require an ac drive signal of 3-6V without dc component, as the latter tends to degrade the material. The device responds to the rms value of the ac signal, and has a threshold of 1-2V rms. Voltages below this level will not turn on the display.

In the following we shall begin by looking at the fabrication of the a-Si FET array and then review its dynamic behaviour in a liquid crystal display. A more extensive discussion is given in references [47] and [48].

Figure 14 shows a schematic diagram of a number of elements in the display panel. A transistor is incorporated in a corner of each element of the array. The FETs are interconnected by means of X and Y buses, G_1, G_2... and S_1, S_2..., linking gate and source contacts, respectively. The drain contact of each transistor is connected to the ITO squares, D. From the section through the panel in Fig.14(b) it can be seen that the liquid crystal material is sandwiched between the substrate carrying the FETs and an ITO coated glass top plate which is normally returned to ground. The liquid crystal element is therefore in series with the drain circuit and behaves electrically as a capacitor C_{LC} with some leakage resistance R_{LC}.

Figure 15(a) shows a section through an individual a-Si device and Fig. 15(b) illustrates the design of the FET in part of the matrix array [48]. As stressed above, all processing is carried out by standard photolithographic techniques and with conventional etches.

The transient behaviour of an FET in the matrix is mainly determined by the capacitative loading of the liquid crystal element. (C_{LC} in Fig.14(b)). This aspect has been investigated with C_{LC} = 10pf, corresponding to ITO elements of 1mm sidelength. When the FET was switched on, the required drive potential across C_{LC} of 3V was reached in 30-40μs. On the other hand, the charge retention on the elementary capacitor in the off-state of the FET is limited by leakage through the liquid crystal material to about 40ms. It is therefore possible, even with the present devices, to address about 1000 lines in this time [48].

We are presently assessing the performance of panels containing 20 x 25 elements, each 1mm² in area. The good uniformity of the transfer characteristics of elements within a panel and their reproducibility in different depositions is encouraging. So far, the information on long term stability of the a-Si devices is still somewhat limited. In a test an element has now been run at 100 Hz with $V_s = \pm 10$V and $V_G = 15$V for 18 months, i.e. for about 5×10^9 switching operations. There has been no sign of deterioration or change in transfer characteristics of this device, which is unpassivated and unencapsulated.

5.3 Application of a-Si FETs in Logic Circuits.

Recently, MATSUMURA, HAYAMA and co-workers showed that an integrated inverter circuit [50] and an image sensor [51] can be fabricated from a-Si FETs. The devices used in their work were made from a-Si deposited in a dc glow discharge and with low pressure CVD SiO_2 as the gate insulator [51].

Although these FETs were relatively leaky and had a slow turn-on they demonstrated the feasibility of using the a-Si technology in these circuits. At the same time work in our laboratory has been concerned with similar applications [52], initially aimed at providing integrated a-Si drive circuits for the liquid crystal display panels discussed above.

Fig.16a shows a section through an integrated invertor and also its lay-out in plan view. The input voltage is applied to the gate of the FET, the source is connected to ground and the output taken from the drain connection. To obtain the appropriate value of load resistance a doped a-Si layer, about 250A thick and about 3×10^3 Ω/□ , was deposited. This was etched away from the source-drain gap of the FET after the top Al metallisation, leaving doped a-Si under the source and drain, which had the added advantage of improving the electrical contact at these electrodes.

The dashed curve in Fig.16b shows the transfer characteristics of such a device having a load of approximately 30MΩ and measured with a supply potential of 15V. The inverter logic is clearly seen: the output changes from about 14.5 to 2V as the input swings from about 5 to 15V. The full line in Fig. 16b shows the characteristics of three such devices connected in series. As well as sharpening the characteristics this demonstrates the important point that the output from one device can be successfully used as the input for successive stages.

By simple extension of the above basic design, logic circuits such as NAND and NOR gates as well as bi-stable multivibrators have been produced [47][52]. As mentioned previously, one of the primary aims of our present work is to investigate the possibility of drive circuits for the liquid crystal panels. Of particular importance in this respect is the fabrication of a shift register to address sequentially the gate buses G_1, G_2,..... in Fig.14. Recently a four stage shift register using a-Si FETs has been made [47][52] in which each stage can shift a 20ns pulse by 10ms. All the circuits mentioned in this section are slow by crystalline standards. At present they are limited to the kHz range, although it must be emphasized that the exploratory a-Si devices described were in no way optimised for speed of response.

5.4 Addressable Image Sensing Elements.

In this section we review the work of MATSUMURA et al [51] and our results on the a-Si image sensors [52]. The circuit used by both groups is shown in the top part of Fig.17 and is that originally suggested by WEIMER et al[53] . Light incident on the a-Si photoconductor charges up the capacitor whilst the FET is off. The FET is then pulsed on and the capacitor discharges rapidly, providing an output current pulse the magnitude of which is a function of the light intensity. Figure 17 shows the magnitude of the output current pulse as a function of light intensity for gate pulse frequencies of 2, 20 and 40 Hz [52]. The output current at 20 Hz, for example, varies by over an order of magnitude as the light intensity is varied from 10 to 1000 lux. These relatively large changes in output current suggest that operation with a grey scale should be feasible.

Further work on this potentially important application is presently being carried out in a number of laboratories throughout the world.

6. Doping in the Amorphous Phase.

This section is concerned with substitutional doping of a-Si in the glow discharge plasma and also by ion implantation. The possibility of efficient doping in the a-phase was demonstrated by the author and P.G. LeComber in 1975 [26][27] and led to the first a-Si p-n junction [54]. This development has removed one of the main limitations of a-semiconductors and opened up exciting possibilities for both fundamental and applied work.

6.1 Control of Electrical Properties of a-Si by Gas Phase Doping

The mechanism of substitutional doping in an a-semiconductor differs basically from that in the crystalline material, because changes in electrical properties are brought about primarily by changes in the gap state occupation. If, for example, N_D substitutional donors are incorporated, practically all the excess electrons will condense into empty gap states near the Fermi level, displacing the latter towards ε_c by an amount $\Delta\varepsilon_f$. For sensitive doping $\Delta\varepsilon_f$, which is of the order of $N_D/g(\varepsilon_f)$, should be as large as possible; a low level of gap states is therefore an essential condition. The field effect measurements discussed in Sect.3 suggest that preparation by the glow discharge technique should be a most promising approach. It was in fact on the basis of these results that we started the first doping experiments in 1975. Reference to Sect.3.3 explains the reason for the insensitivity to doping of evaporated a-semiconductors. Although it may be possible to incorporate donors or acceptors into the material, the overall $g(\varepsilon)$ is too high to allow much change in the Fermi level position and consequently in the electrical properties.

Gas phase doping in glow discharge Si or Ge is carried out by introducing small but accurately controlled amounts of phosphine (PH_3) or diborane (B_2H_6) into the reactor by means of the gas handling system shown in Fig.3 (Sect.2.1) The gaseous doping ratio D is defined as the ratio of the number of phosphine (or diborane) to silane molecules in the mixture. Ratios as low as 10^{-6} can be obtained by pre-mixing in the reservoir R (Fig.3), whereas for D values exceeding 3×10^{-4}, direct electronically controlled mixing during the deposition run is sufficiently accurate.

Figure 18 summarises the doping dependence of the room temperature conductivity σ_{RT} in glow discharge Si. σ_{RT} is plotted against the doping ratio - on the right side of the diagram for phosphorus doping and on the left for boron doping; the centre refers to the undoped material. The results illustrate the remarkable control of the conductivity that can be achieved in

carefully prepared specimens. Curve (a) represents the typical dependence of specimens prepared in the deposition unit shown in Fig.3. With $D = 10^{-6}$, σ_{RT} on the n-side has been increased by an order of magnitude over that of the undoped specimen, and the highest doping ratio of 10^{-2} leads to $\sigma_{RT} = 2 \times 10^{-2}(\Omega cm)^{-1}$.

Light boron doping first moves ε_f into the centre of the mobility gap, where σ_{RT} reaches its 'intrinsic' value of about $10^{-12}(\Omega cm)^{-1}$. The specimen then turns p-type and the rapid rise of σ_{RT} with further boron doping indicates that hole conduction has taken over, which is also confirmed by the sign of the thermoelectric power and by the field effect.

From measurements of the temperature dependence of σ it is concluded that, by doping, the Fermi level position can be controlled over about 1.2 eV, essentially between the onset of the electron and hole tail states. This has also been confirmed by photoemission measurements [55]. The information summarised in Fig. 18 leaves little doubt that systematic control of the electronic properties of glow discharge Si by P or B doping is a very real possibility.

Curve (b) included in Fig. 18 shows the originally published doping results [27] obtained with specimens from a smaller capacitatively coupled system. Comparison with (a) suggests that doping in the larger deposition unit of Fig.3 is more effective, particularly on the n-side.

Figure 18 also includes results for microcrystalline Si specimens prepared directly in the glow discharge (curves c,d and e). These will be discussed in Sec.8.2.

6.2 Doping by Ion Implantation.

In the field of crystalline semiconductors ion implantation has become an important doping technique. It appeared, therefore, of fundamental and applied interest to explore the feasibility of this technique in the doping of an amorphous semiconductor. In a paper presented at the 1977 Edinburgh Conference [28] we were able to show (in collaboration with colleagues at the Max-Planck Institute in Heidelberg) that substitutional doping of a-Si by boron and phosphorus implantation is indeed possible. Figure 19 summarises the results of more recent work [29]. It shows the dependence of σ_{RT} of glow discharge a-Si on the implanted densities of phosphorus-, boron- and alkali- ions (curves P_I, B_I and A_I respectively). For comparison, curves P_G and B_G, representing gas-phase doping, have been included. Evidently, ion implantation can be used to control the electrical properties of a-Si over the same range as gas-phase doping, although Fig. 19 indicates that the latter is considerably more efficient. Similar results have been obtained with other group III and V ions [29].

The curve denoted by A_I represents the results of interstitial doping by the alkali ions Na, K, Rb and Cs [56]. It is interesting to note that in spite of the different ionic masses the conductivity changes produced by these ions are practically identical. Interstitial doping by Li ions and by in-diffusion of an evaporated Li layer have been investigated by BEYER and FISCHER [57]. The major disadvantage of Li as an interstitional donor lies in the limited thermal stability of the electrical properties of the doped specimen. This is overcome by the use of the heavier alkali ions which lead to stable properties up to 400°C [56].

Compensation experiments using ion implantation have led to encouraging results and it has been shown that viable a-Si p-n junctions can be made by this technique [29]. Recent work on the use of implantation doping in the production of a-Si solar cells has been reported in a paper at the 1981 Grenoble Conference [58]. The problem of implantation damage in a-Si is discussed in Ref. [29] and has also been investigated by MÜLLER and LECOMBER [59] using irradiation with chemically inactive species.

7. The Amorphous Silicon Junction and its Applications.

The effective doping of a-Si discussed in the last section has opened up interesting possibilities for the application of this material in a-junction devices. A particular attraction lies in cheap, large-area devices and it is this aspect which has stimulated world-wide developments in the a-Si field. In this section we shall begin with an introduction to the basic properties of the a-barrier and junction and then go on to discuss some of the junction devices that have been investigated during the last few years.

7.1 Formation and Electronic Properties of the Metal/a-Si Barrier and the a-Junction.

The a-barrier differs basically from its crystalline counterparts because the net space charge in the barrier region is determined not only by ionised impurities, but also by the density of state distribution in the mobility gap. Useful insight into the formation and properties of the metal/a-Si barrier and their dependence on doping levels, has been gained from model calculations [60] based on the experimentally determined density of state distribution discussed in Sect.3. Knowing the net charge in localised states in addition to that in ionised donors and acceptors, the overall space charge distribution could be obtained as a function of electron energy. A step-by-step solution of Poisson's equation then led to the spatial profile $\epsilon_b(x)$ of the barrier.

In undoped or weakly doped material, where the net space charge is mainly determined by the localised state contribution, $\varepsilon_b(x)$ differs considerably from the parabolic shape often considered in the crystalline case, assuming a constant charge distribution qN_D^+. The barrier on undoped a-Si is characterised by a long, shallow initial part (as seen from the specimen volume), going over into a sharply rising profile near the metal contact. This is a direct consequence of the increase in $g(\varepsilon)$ towards the ε_y-peak (see Fig. 11). In medium and highly doped material, the contribution of the ionised impurities becomes the dominant factor in the space charge distribution and $\varepsilon_b(x)$ approaches the parabolic profile. The model calculations have also been extended to a-Si p-n junctions for various doping levels [60].

The differential capacitance C of the metal/a-Si barrier and its bias- and frequency- dependence can be calculated from the above space charge distributions. Measurement of C then provides an interesting check of the model calculations and also of the underlying density of state distribution. This approach has been used by SNELL et al [61] who showed that the observed features of the capacitance measurements on Au/a-Si barriers can be explained satisfactorily in terms of the analysis. A similar investigation of Pt/a-Si barriers has been described by Beichler et al [62]. This work confirms the strong frequency dependence of C, associated with the contribution to the barrier space charge of deep lying localised states. But unlike SNELL et al, the above authors do not find an increase of C in reverse bias at very low frequencies, where most of the deep states can reach their steady state occupation.

7.2 Junction Configurations and High Current Diodes.

The work during the last few years has shown that the most promising a-Si junction configurations are those in which the main part of the device consists of an undoped or lightly doped n-type layer, 0.5 - 1μm in thickness. The junction is formed by thin (≈100Å), highly doped n^+ and p^+ films deposited on either side of the central layer to form structures such as n^+-i-p^+, n^+-ν-p^+ or p^+-i-n^+. In this notation 'i' and 'ν' refer to undoped and lightly phosphorus doped central layers respectively; the sequence is in the order of deposition of the multi-layer film.

The operation of such devices is critically dependent on the lifetime of excess carriers, injected into the low conductivity central region from the highly doped layers, or produced by photogeneration. In this section we shall be concerned with the first mechanism. Fig. 20 for a symmetric n^+-i-n^+ structure, used in the study of S.C.L. current flow (Sect. 3.5)[34], illustrates the remarkable injecting properties of thin n^+ contacts on undoped a-Si. It can be seen that the current density J is increased by four orders of magnitude when a few volts are applied across the device. Also the properties of the injecting contacts are accurately reproducible, as shown by the symmetry of the characteristics.

In n^+-i-p^+ or related configurations strong double injection takes place into the central region under forward bias and the density of excess carriers greatly exceeds the thermal equilibrium densities. We have investigated the common lifetime τ of excess carriers under these conditions [63][64] using a junction recovery method, similar to that often employed for corresponding crystalline devices. The results show that at high injection levels τ is about 1μs for the above mentioned a-Si configurations. At a reduced current level of $10^{-2}Acm^{-2}$, τ approaches values between 20 and 30μs. It must, however, be stressed that τ does not represent the 'free' lifetime, because the injected carriers interact through trapping and thermal release with the band tail states. The latter are in quasi-thermal equilibrium with the extended electron states and the measured lifetime includes therefore the integrated localisation time in these states. Exactly the same conditons apply to drift mobility measurements on excess carriers, so that the two measured quantities, τ and μ, should be combined in consistent estimates of drift and diffusion lengths.

One of the attractive features of the amorphous junctions lies in the fact that their profile can be controlled continuously during deposition from the gas phase. This may eventually prove to be an important factor in optimising junction performance for particular applications. The approach has been used in an attempt to improve and optimise the forward current in a-Si junctions [65]. Some of the most promising results were obtained from structures of the n^+-ν-p^+ type, about 0.75μm thick and deposited on stainless steel foil. Figure 21 shows a series of characteristics plotted on a semi-logarithmic graph of the current density J against the applied potential V. It can be seen that the current carrying capacity of the n^+-ν-p^+ devices in the forward direction increases systematically with the doping level of the central region; ν = o represents a n^+-i-p^+ junction. The d.c. characteristics terminate at the loading where thermal runaway sets in. For ν = 40 vppm this is over 20 A cm^{-2} and steady current densities of up to 40 A cm^{-2} have been observed. The reverse characteristic for the ν = 40 vppm specimen shows that the rectification ratio at V = 1V (the approximate barrier height) is about 5 x 10^4. A transition to Zener breakdown is observed at reverse voltages which depend on the doping level. Ideality factors of about 1.5 were found both from the dark characteristics and from photovoltaic experiments. These results are encouraging and suggest that cheap a-Si junction devices may find applications in cases where some relaxation in electrical characteristics from those of crystalline junctions will be acceptable.

7.3 The a-Si Photovoltaic Junction.

At the present time the development of photovoltaic devices for solar energy conversion is a challenging problem. It is likely that a stable thin-film material will ultimately provide the best solution to the large-scale production of cheap, reasonably efficient photovoltaic junctions for use as a supplementary energy source. CARLSON and WRONSKI [66] showed in 1976 that glow discharge a-Si could be successfully applied in photovoltaic cells. Since that time many industrial laboratories have entered the a-Si solar cell field, which has become highly competitive.

In the following we shall confine ourselves to two basic material aspects which have important implications for the development of viable p^+-i-n^+ photovoltaic junctions. Figure 22 shows a desirable electronic structure through the thickness of a good a-Si p^+-i-n^+ cell. The device is deposited on the stainless steel substrate S and the light enters through the conducting indium-tin oxide (ITO) film, (∿ 500Å thick), which also acts as a simple anti-reflection coating.

In the extraction of the photogenerated carriers both diffusion and drift in the built-in field play a part. It is therefore relevant to consider the diffusion length L and the drift length δ of the excess carriers. These quantities are given by

$$L = \left(\frac{kT}{|e|}\mu\tau\right)^{1/2} \qquad \text{—— (4)}$$

and

$$\delta = \mu\tau E \qquad \text{—— (5)}$$

Both involve the carrier mobility; with a drift mobility of excess holes lying between 10^{-4} and 10^{-3} $cm^2V^{-1}s^{-1}$, about two orders of magnitude smaller than for electrons, it is likely that L_h and δ_h are critical parameters in the performance of photovoltaic devices. Direct measurements of L_h were made by STAEBLER [67] who investigated the collection of photogenerated holes as a function of intrinsic layer thickness on a wedge shaped specimen. He estimated an upper limit to L_h of 350Å. This appears to be rather low in view of more recent measurements by the P.E.M. effect [68] and by the surface voltage technique [69], which gave values of about 0.1μm and 0.4μm respectively.

The hole diffusion length can also be obtained from mobility and lifetime

measurements, using Eqn.(4). For example, if it is assumed that the junction recovery results, mentioned in Sect.7.2, can also be applied to photogenerated carriers in the i-region then, at the appropriate current density (10mA cm^{-2}), τ lies between 20 and 30 μs. Combining this with an average hole drift mobility of 5 x10^{-4} $cm^2V^{-1}s^{-1}$ gives $\mu_h\tau \approx 1.3 \times 10^{-8} cm^2V^{-1}$ and $L_h \approx 0.2\mu m$. Finally, the recent work of ABELES et al [70] on a-Si Schottky barriers leads to L_h values between 0.1 and 0.2μm (for $d < 1\mu m$). It appears therefore that on the basis of presently available information, hole diffusion lengths are a fraction of the thickness of the intrinsic region in present photovoltaic devices.

As both L_h and δ_h are determined by the $\mu_h\tau$ product, it is important to keep a close check on this quantity in optimising material properties. A useful transient method has recently been described [58], whereby $\mu_h\tau$ and E_o of the p^+-i-n^+ junction can be determined under operating conditions. Figure 23 shows the arrangement. A short light flash from an Ar spark source is used to probe the steady state existing in the device without appreciably perturbing it. The metal bottom electrode B of the cell is connected to the load resistor R_L, the ITO top contact T to the potential V_T. The external potential V across the cell can be changed by positive or negative V_T, and/or by steady illumination, which increases $|V_B|$. To a reasonable degree of approximation, the average field in the i-region is given by

$$E \simeq E_o + \frac{V}{d} = E_o + \frac{\pm|V_T| - |V_B|}{d} \qquad (6)$$

In the experiment, highly absorbed blue or green probe flashes are used to generate electron-hole pairs near the electrode T. Electrons are rapidly extracted and excess holes drift through the i-region in the internal field E. By making R_L sufficiently large (> 0.5MΩ) the integrated charge displacement Q of the holes can be measured directly on the oscilloscope connected

across R_L and investigated as a function of E. The ratio Q/Q_{sat}, where Q_{sat} represents the total extracted charge as $E \to \infty$, is given by the well-known Hecht-formula [71]

$$\frac{Q}{Q_{sat}} = \frac{\mu_h\tau E}{d}\left[1 - \exp\left(-\frac{d}{\mu_h\tau E}\right)\right] \qquad (7)$$

This relation is based on a simple model in which the range of the generated holes is limited by deep trapping. It should be applicable to the primary transient photocurrent observed here; the small excess carrier densities used and the low pulse repetition rate ensure that any trapped space charge does not perturb E to any extent.

The experimental points in Fig.24 represent measurements of the integrated pulse height as a function of V/d (see Eqn.6); the solid line is a computer fit of Eqn. 7 to the experimental data, which determines the Q/Q_{sat} scale and the $\mu_h\tau$ value, 1.0 x $10^{-8} cm^2V^{-1}$ in this case. Also, from the intercept of the fitted curve with the V/d axis we obtain a value of $E_o \approx 13$ $kVcm^{-1}$. As a check μ_h, τ and E_o were also determined from time resolved transient measurements [58] on the same series of solar cells. For the above junction, $\mu_h\tau$ was found to be 1.1 x $10^{-8} cm^2V^{-1}$ and $E_o \approx 11$ $kVcm^{-1}$, in good agreement with the experimentally simpler pulse height experiments.

The results suggest that in a reasonably efficient p^+-i-n^+ photovoltaic cell, with a fill factor approaching 0.6, the field E_o lies between 10 and 20 $kVcm^{-1}$. Under short-circuit conditions, the drift distance $\mu_h\tau E_o$, is therefore 1-2μm, appreciably longer than the diffusion length. However, as the external load connected across the illuminated cell is increased, the internal field is reduced below its maximum value E_o and range limitation for holes will set in as δ approaches the specimen thickness d. It is important, particularly for a satisfactory fill factor, that the limiting condition $\delta \approx d$ should correspond to as low a field as possible. When the conversion efficiency

for a batch of solar cells is correlated with the device thickness, it has been found by several groups that with the presently available material there is an optimum value at $d \sim 0.5\mu m$. We believe that this is a direct consequence of the range limitation for holes and suggests that material improvements in this direction should be of importance in the a-Si solar cell development.

The second topic in this section concerns the problem of geminate recombination in a-Si and its possible fundamental limitation of solar cell performance. In a geminate recombination process, the photogenerated electron thermalises and then recombines with the hole from which it was excited. Such pairs do not contribute to photoconduction and therefore reduce the overall generation efficiency per absorbed photon, which will be denoted by η. The most detailed theory of geminate recombination and its dependence on applied field was originally given by ONSAGER [72] and the results were used to interpret photogeneration in a-Se [73], anthracene [74] and other organic photoconductors. The theory considers the photoexcited electron in the Coulomb field of the hole. The spatial extent of the interaction between the charges is defined in terms of the Coulomb radius r_c at which the potential energy in the well equals kT. In a-Si, $r_c \simeq 50\text{Å}$. The excited electron thermalises within a distance r_o and the relative values of r_c and r_o, as well as E, determine whether separation or geminate recombination of the pair is most likely to occur. Figure 25(a) shows the characteristic field dependence of η predicted by the Onsager theory for a-Si with $r_c = 50\text{Å}$. The curves refer to r_o values of 30, 40, 90 and 300Å, which give low-field efficiencies between 0.2 and 0.9.

Recently, MORT and his collaborators have investigated geminate and non-geminate recombination in a-Si, by combining xerographic discharge measurements and delayed-collection field techniques [75][76][77]. The results show that, depending on specimen preparation, η ranges from 0.44 to 0.55 and that the field dependence of η fits the Onsager curves, such as those in Fig. 25(a),

suggesting r_o values from 45Å to 80Å. In a subsequent paper, CHEN and MORT [78] reached the somewhat controversial conclusions that (i) geminate recombination presents a fundamental limitation to photogeneration in a-Si and (ii) that carrier lifetime limitations are unimportant in present photovoltaic cells.

The first conclusion is not supported by results on photovoltaic cells obtained in several laboratories working on such devices. (e.g. [79][80] Collection efficiencies of 0.8 or above are commonly observed in the green part of the spectrum, substantially larger than the maximum value of about 0.65 calculated by Chen and Mort from $\eta = 0.55$. This discrepancy implies that the generation efficiency in a-Si should generally be much closer to unity than is suggested by the Xerox experiments.

Further evidence, pointing in the same direction, is provided in Fig. 25(b) from some of our recent work [81]. The curves show the shape of the field dependence of the primary photocurrent in p^+-i-n^+ junctions under steady illumination with photon energies close to and above the optical gap of a-Si. i_{ph} was measured under short-circuit conditions and the built-in field E_o was increased or decreased by an applied potential as described above (Eqn. 6). The i_{ph} scale is in arbitrary units and the curves have been separated vertically to show conclusively the absence of any measurable field dependence for $E > 20\text{kV cm}^{-1}$. At smaller fields, the lifetime limitation of the holes, discussed earlier, is the most likely cause for the decrease in i_{ph}. The quantum efficiency measured independently on these devices, lies between 0.9 and 1 and is therefore consistent with the observed saturation of i_{ph}. These and other results strongly suggest that there is little or no evidence for geminate recombination in a-Si devices prepared in several laboratories. It appears therefore unlikely that this mechanism should present a serious limitation in the photovoltaic efficiencies ultimately achievable.

7.4 Application to Electrophotography and Image Tubes.

The high photosensitivity of a-Si throughout most of the visible spectral region has stimulated exploratory work, particularly in Japan, on its application in electrophotography and in image tubes of the Vidicon type. An essential requirement for the operation of both these devices is good photoconductivity, combined with a high dark resistance which should normally be larger than the 10^{12} Ωcm bulk resistivity measured for 'intrinsic' a-Si. (See Fig. 18).

SHIMIZU and his collaborators [82][83][84] have investigated the use of reverse biased p-i (or n-i) junctions for these applications as well as thin, insulating dielectric blocking layers. Some of the main results will now briefly be summarised. Starting with the work on a photoreceptor for electrophotography, the upper diagram in Fig. 26 illustrates the specimen configuration for use with positive corona charging. A p- type a-Si layer, about 0.2μm thick, is deposited from 350 vppm of diborane in silane on to the grounded Ni-Cr film. For the given electric field, this doped layer prevents the injection of excess electrons from the substrate. It is followed by 6μm of 'intrinsic' a-Si, which is deposited with a small diborane content (10 vppm) to move ε_f to the intrinsic position in the centre of the mobility gap (see Fig.18). The dependence of the surface potential V_s on time is also shown in Fig.26. The rate of dark decay is now acceptable for electrophotographic application and the photodischarge curves obtained with 600 nm light at the given intensities show that no residual charge remains after illumination. In recent experiments [82] the surface potential at t = o has been increased to about 400V in a 10μm a-Si layer, which allows development with a conventional toner.

These results are encouraging and suggest that a-Si may find application as a highly sensitive photoreceptor in electrophotography. Further attractive features in this connection are the mechanical hardness and the non-toxicity of the material.

In a Vidicon image tube the unelectroded surface of the photoconductive layer is scanned by a low energy electron beam which stabilises it to cathode potential. Fig. 27 illustrates the structure of an a-Si Vidicon target investigated by SHIMIZU et al [82][84]. The image is focussed on to the glass disc which carries a positive biased transparent ITO film. A n-type blocking layer (doped with 50 vppm of phosphine) prevents injection of holes from the ITO. As an alternative solution, a blocking layer consisting of 300Å of glow discharge silicon nitride was found to be successful. The main part of the target consists of lightly B-doped 'intrinsic' a-Si, up to 4μm in thickness (to reduce capacitative lag). Finally, the scanned surface is covered with a thin (≈ 1000Å) 'electron blocking' layer of Sb_2S_3 (or other chalcogenide), which tends to improve the resolution of the picture. The a-Si Vidicon performance compares favourably with that of the more conventional tubes: the resolution is better than 800 TV lines for the 1" a-Si tube and the decay lag in the picture from a 4μm thick target is about 5% after 50ms (3 fields).

7.5 Application to a Memory Device.

In this section we should like to discuss briefly a new a-Si memory device [85] developed jointly by the Edinburgh and Dundee groups. It is an electrically programmable, non-volatile memory element which in terms of speed, retention time, operating voltages and stability compares very favourably with crystalline MNOS (metal-nitride-oxide-semiconductor) or FAMOS (floating-gate-avalanche-metal-oxide-semiconductor) devices currently used for non-volatile programmable storage.

The most promising configuration investigated so far is of the p-n-i type. The layers are deposited on a stainless steel substrate, giving a total device thickness of between 0.5 and 1.0μm. A series of Au or Al dots is then evaporated onto the surface to form the top contacts.

After an initial forming step the structure operates permanently as a non-volatile memory. Figure 28 shows a typical set of static (d.c.) current/applied voltage characteristics. Immediately after forming, the device is in its on-state so that small positive and negative voltages trace out curve AB; on-state currents of 10 mA or more are generally observed. On increasing the reverse potential (i.e. a negative voltage applied to the p-doped region) a reverse threshold voltage V_{ThR} is reached beyond which the device switches to an off-state with a resistance of the order of 1MΩ, represented by the characteristic CD. The reverse threshold $V_{ThR} = 1V$ and the off-state is stable for voltage swings of ± 4V. If the forward potential is now increased beyond a value of V_{ThF}, the forward threshold voltage, the device switches back into its high conductivity state AB, in some cases through an intermediate state such as E or F.

The above cycle has been repeated up to 10^5 times without observable changes in characteristics or threshold voltages. Devices set in on- and off-states have been monitored for several weeks without detectable change in either characteristic. Operation at temperatures of up to 180°C shows little change in the threshold voltages.

The dynamic characteristics of the p-n-i devices has been investigated with 10V forward and reverse pulses of 100 ns duration. The experiments demonstrate the important result that both the on-off and off-on transitions are completed within 100 ns and that there appears to be no observable time delay in the switching response. It is estimated that the energy absorbed during either transition is extremely low, typically in the range 10^{-6} to 10^{-8}J.

The mechanisms underlying the switching phenomena described above are unknown at present. However, it will be useful to draw some comparisons with other related devices. Much attention has been given over the past 10-15 years to memory switching devices fabricated from multi-component chalcogenide glasses in which the reversible memory action is associated with the growth and destruction of a crystalline filament [86,87]. The switching phenomenon in the a-Si structures reported here is clearly very different, at least operationally. The most obvious difference is the completely non-polar character of switching in chalcogenide glass devices, in contrast to the marked polarity-dependence of the a-Si memory switches. More importantly perhaps, the switching times for the a-Si device are much faster compared with those in chalcogenide devices, which are at least several milliseconds long. In addition the energy involved in the a-Si switching process is considerably lower

8. Micro-crystalline Si Produced in the Glow Discharge Plasma.

During the last two years the possibility of depositing thin films of microcrystalline (μc) Si directly in the glow discharge has aroused considerable interest. On the fundamental side this material, which we shall denote by gdμc Si, permits an extension in the study of the electronic properties just beyond the a-phase. The films possess very limited long range order, with crystallite sizes of up to 60Å; the latter can be controlled to some extent by the preparation conditions. On the applied side, the attractive feature is that simply by turning a tap during an a-Si deposition run, one can produce a highly conductive gdμc surface layer which could be most useful, for example, in the photovoltaic development.

In the following sections we shall summarise and discuss some of the recent work in this new field.

8.1 Preparation and Structure of gdμc-Si.

The possibility of depositing a microcrystalline semiconductor specimen in a glow discharge plasma was first recognised by VEPŘEK and MARAČEK in 1968 [88] using chemical transport in a hydrogen plasma. This method offers a

versatile approach for the study of the kinetics of the silicon-hydrogen system [89] and of the conditions for the direct deposition of a μc film. The work of the ZÜrich group suggested that stable nuclei for μc growth are likely to be formed under plasma conditions whereby a chemical equilibrium is approached at the plasma-solid interface [90][91].

This condition is expressed by the reactions [90]

$$SiH_x(g) \rightleftarrows Si(s) + xH \text{ (plasma)} \qquad \text{—— (8)}$$

The forward reaction (left to right) represents the deposition of the gaseous Si-H fragments to form the a-Si film and add gaseous hydrogen to the surrounding plasma. In the reverse direction the interaction of the plasma with the solid Si film leads to erosion. Normal deposition conditions for a-Si are such as to make the forward reaction the dominant one, so that the system is far from chemical equilibrium.

Work by several Japanese groups [92][93][94] showed that μc Si specimens can also be produced in the silane glow discharge reactors described in Sect.2. In this case chemical equilibrium is approached by strong hydrogen dilution and an increase in the normal level of r.f. power. Evidently the former will enhance the reverse reaction in Eqn.(8); the observed deposition rate is slowed down to 0.1-0.2Å s^{-1}, in spite of the increased r.f. power, indicating that the system is fairly close to a dynamic equilibrium.

Under these conditions stable nuclei are formed which stimulate the growth of a gdμc-Si layer.

8.2 Conductivity.

In this and the following sections we shall present the results obtained on a series of undoped and n-type gdμc Si specimens [95]. They were deposited in the system shown in Fig.3, with an excitation frequency of 40MHz and an r.f. power of 20-30W. The gas mixture contained 2-3% of silane in hydrogen with

the required addition of phosphine for the n-type films. The average crystallite size δ was determined for each deposition run from the half-width of the (111) electron diffraction ring by means of the Scherrer formula.

The σ_{RT} vs. doping level curve for these specimens has been included in Fig.18 (Sect.6). The curve, denoted by (c), refers to specimens with $\delta \approx 50$Å; smaller δ values give conductivities lying below (c)[95]. It can be seen that for undoped gdμc Si $\sigma_{RT} \approx 10^{-2}(\Omega cm)^{-1}$, although lower values, also corresponding to $\delta \approx 50$Å, have been observed in some deposition runs. In phosphorus doped specimens, σ_{RT} lies over two orders of magnitude higher than in a-Si and reaches values around $20(\Omega cm)^{-1}$ at the higher D.

Boron doped μc specimens are more difficult to prepare in the glow discharge plasma. Curve (d), from the work of MATSUDA et al [96] refers to p-type μc material prepared at an r.f. power of 80W, appreciably higher than for n-type specimens. Curve (c) recently obtained by HAMASAKI et al [97] increases the σ_{RT} range further, approaching values of $8(\Omega cm)^{-1}$ on the p-side at the highest doping ratios. It may be significant that these authors used a magnetic field to confine the glow discharge plasma.

Before leaving the subject of conductivity we should like to add a brief comment about the use of SiF_4 in the glow discharge, instead of the SiH_4 considered so far. The presence of fluorine, a well-known plasma etchant, will enhance the reverse reaction (erosion) in Eqn.(8) and is likely to lead towards chemical equilibrium and a μc structure with little hydrogen dilution and probably at lower power levels. The x-ray and conductivity results of MATSUDA et al [93]show that this is indeed the case. These results also suggest that the high (apparent) doping efficiency claimed in specimens deposited from SiF_4 + 10% H_2 [98] on the basis of conductivity measurements, is mainly due to their microcrystallinity. This throws considerable doubt on the conclusion by MADAN et al [98] that these results refer to a-Si, but with an appreciably lower density of states than in specimens prepared from a silane glow discharge.

8.3 The Hall Effect.

The work of LECOMBER et al [44] showed that in a-Si the sign of the Hall effect is anomalous - n-type specimens gave a positive Hall constant and a negative sign was observed for p-type a-Si. Clearly, the crystalline interpretation of the Hall effect can no longer be applied to transport in the random phase region of an a-semiconductor where the mean free path of the charge carriers has been reduced to a few atomic spacings by the disorder. The theories that have been developed take account of the 'microscopic' details of the transport and show that the magnitude and sign of the Hall constant will depend on the local geometry in the sites involved [42] and also on the nature of the local electronic states [43].

In the present work on undoped and n-type gdμc Si it was found without exception that the Hall constant had the negative sign expected from crystalline transport theory, even in specimens with the smallest δ values. This suggests that with the limited long range order introduced, the mean free path of the electrons becomes sufficiently long for the description in terms of classical electrodynamics to be applicable. We have therefore used the simple formula $R_H = (ne)^{-1}$ to obtain an approximate value for the carrier density n from the experimental Hall constant R_H.

In Fig.29 n has been plotted as a function of the doping ratio D for gdμc Si specimens and several thermally crystallised a-Si films (thμc) [95]. U refers to nominally undoped gdμc specimens. n rises almost linearly with the density of PH_3 molecules in the gas phase and is independent of the method of crystallisation and also, within the limited range investigated, of the crystallite size. If one compares the gaseous doping ratio D with n/N_{Si} in the solid, one finds about 0.5D for the latter, indicating that doping in gdμc Si must be reasonably efficient.

From the values of n and the corresponding conductivities the Hall mobility μ_H can be deduced. For the gdμc Si specimens the room temperature values of μ_H generally lie below $1 cm^2 V^{-1} s^{-1}$ and are largely independent of the doping level. However, μ_H depends on crystallite size, as shown by the upper part of Fig.30(R_H - negative). In spite of the scatter in the present results, μ_H extrapolates to zero at a critical grain size of about 20 Å. Below $\mu_H = 0$, the open circle denotes a typical result for a lightly phosphorus doped a-Si specimen [44], corresponding to an anomalous positive R_H. The magnitude of μ_H for the a-specimen is in agreement with the predictions of the FRIEDMAN theory [42], but no physical significance should be attached to the corresponding crystallite size of about 12Å. It may perhaps be relevant that δ values between 10 and 12Å are generally found when the Scherrer correlation graph is extrapolated to the diffraction line width observed with a-Si specimens.

The results given in Fig.30 are of considerable interest: they suggest a limiting size of the ordered regions, 20-30Å, for which the transport at the mobility edge of the material can be described in terms of the normal crystalline theory. Once the extent of the ordered regions falls below that limit, then the above microscopic theories, become applicable.

What is the fundamental reason for the greatly increased carrier density in the μc phase? We originally suggested [95] that the order introduced is sufficient to affect the extent of the localised electron tail states. In a-Si this is about 0.18eV; field effect measurements near the mobility edge of gdμc Si suggest that the width of the tail states has been considerably reduced, or that they may have been removed altogether.

If the interpretation of these results is correct, the increase in n can be understood. Whereas the rapidly rising tail state distribution in a-Si limited $\varepsilon_c - \varepsilon_f$ to about 0.15eV even at the

highest doping levels, the suggested 'delocalisation' in the μc material allows ε_f to move close to the current path at ε_c with phosphorus doping. This is clearly shown by the experimental results in Fig. 33 and fully explains the observed increase in n and σ.

8.4 Thermoelectric Power.

A systematic study of the temperature- and doping-dependence of the thermoelectric power S in gdμc Si has recently been carried out [100]. One of its aims has been to determine whether a consistent interpretation of the results can be given in terms of crystalline semiconductor theory. Figure 31 summarises the experimental results on a graph of S vs. $10^3/T$. The solid lines represent calculated S-curves which will be discussed below. The numbers refer to the specimens used: 1 is an undoped gdμc Si film and in specimens 2 to 6 the doping ratio is increased from 5×10^{-5} to 10^{-2}. Specimen 7 is a doped thermally crystallised film and 8 an a-Si specimen included for comparison.

The main point brought out by Fig.31 is that all the μc specimens show a similar temperature dependence which varies systematically with the doping ratio. However, comparison with a typical curve for a-Si (specimen 8) shows that there is a basic difference between the temperature dependence of S in the two cases.

The thermoelectric power for a non-degenerate semiconductor is given by the well-known expression:

$$S = -\frac{k}{|e|}\left[\ln\left(\frac{N_c}{n}\right) + A_c\right] \qquad \text{—— (10)}$$

where N_c is the effective density of states near the bottom of the conduction band and A_c the heat of transport. The latter, normally taken as temperature independent, accounts for the contribution to S of electrons distributed in states above the conduction band edge ε_c and will depend both on state distribution and transport.

As recognised in earlier work on thermally crystallised a-Si [99], it is essential in the interpretation of the thermoelectric power data to take account of the temperature dependence of N_c. Clearly, if n does not vary greatly with T, which is the case for the doped μc specimens, then according to Eqn.(10), S(T) should reflect $N_c(T)$. This is not normally evident in the results for a-Si, because there n is more strongly activated, obscuring the smaller temperature dependence of N_c.

For crystalline Si, N_c is proportional to $T^{3/2}$. In the present analysis we shall begin with the more general expression

$$N_c = bT^{\nu} \qquad \text{—— (11)}$$

and determine the value of ν from the experimental data.

A stringent test of the consistency of the experimental results in terms of Eqn.(10) consists in plotting $-(|e|S/k)$ against ln(n) at a given temperature, using the value of n determined from the Hall effect. This has been done at different T throughout the range investigated and Fig.32 shows an example at T = 300K. The points define a line having the expected slope of -1; the intercept on the abscissa gives a value for $\ln(N_c) + A_c$, which according to Eqn.(11) equals $\nu \ln T + \ln b + A_c$. From the temperature dependence of the intercept a value of $\nu \simeq 2$ is deduced.

Unfortunately, the analysis cannot separate the terms lnb and A_c; for reasons discussed in Ref.[100], A_c values between 2 and 3 are most likely. At 300K and with $A_c = 3$, $N_c = 3.5 \times 10^{19} cm^{-3}$, close to the value of $2.8 \times 10^{19} cm^{-3}$ for crystalline Si. As a consistency check of the analysis the temperature dependence of S for the μc-specimens has been calculated from Eqns.(10) and (11), using $A_c = 3$ and the experimentally determined n-values. The results are shown by the solid lines 1 to 7 in Fig.31 which successfully reproduce both the temperature and doping dependence of S. This leads to the conclusion that a consistent interpretation of the Hall and thermoelectric power data can be given by conventional semiconductor theory. The only difference lies in the temperature dependence of N_c which could be associated with different state distributions above ε_c in μc and single crystal Si.

Finally, the thermoelectric power data provide reliable information on the temperature and doping dependence of the Fermi level position. Using non-degenerate statistics, Eqn.(10) can be written as

$$\epsilon_c - \epsilon_f = - kT \left(\frac{|e|S}{k} + A_c \right) \qquad \text{—— (12)}$$

Figure 33 shows the room temperature value of $\epsilon - \epsilon_f$ as a function of the doping ratio (expressed in vppm) for $A_c = 3$. $\epsilon_c - \epsilon_f$ vanishes at a doping ratio between 1×10^3 and 2×10^3 vppm, corresponding to an estimated donor density of about $3 \times 10^{19} cm^{-3}$. This is somewhat higher than the limiting density originally determined by PEARSON and BARDEEN [101] for phosphorus doped polycrystalline Si.

9. Concluding Remarks.

In these notes we have attempted to survey significant developments in the field of glow discharge Si, over as wide a range as possible. The close relation between the fundamental studies of the material and the applications has been stressed throughout, because it is this aspect which has largely contributed to the rapid growth of the a-Si field during recent years. It applies in particular to the two major developments considered above , the a-Si FET and the a-Si junction, both of which have opened up a wide range of new and exciting possibilities for application. The common features underlying these developments are the unique properties of glow discharge Si, particularly the low overall density of gap states which at the present time makes it into the most viable a-semiconductor for electronic applications.

As to the future, there is little doubt that with the electronic control achievable, glow discharge Si will remain a useful model material in studies of the fundamental properties of a-semiconductors. The applied developments discussed here are very promising and raise the hope that ultimately a-Si may approach the industrial importance of its crystalline counterpart. However, the history of electronic device developments during the last two decades teaches the need for considerable caution in speculating about the future extent and range of the a-Si development. We believe that one of the decisive factors will be the continued progress in solving the problems of industrialising the glow discharge preparation technique.

References

1. H.F. Sterling, R.C.G. Swann: S.S. Electronics 8, 653-654 (1965)
2. R.C. Chittick, J.H. Alexander, H.F. Sterling: J. Electrochem. Soc. 116, 77-81 (1969)
3. P.G. LeComber, W.E. Spear: Phys. Rev. Letters 25, 509-511 (1970)
4. P.G. LeComber, A. Madan, W.E. Spear: J. Non-Crystalline Solids 11, 219-234 (1972)
5. J.C. Knights: Phil. Mag. 34, 663-667 (1976)
6. J.C. Knights, G. Lucovsky, R.J. Nemanich: J. Non-Crystalline Solids 32, 393-403 (1979)
7. Y. Kuwano, M. Ohnishi: J. de Physique 42, C4, 1155-1164 (1981)
8. B.A. Scott, M.H. Brodsky, D.C. Green, P.B. Kirby, R.M. Plecenik, E.E. Simonyi: Appl. Phys. Letters 37, 725-727 (1980)
9. B.A. Scott, M.H. Brodsky, D.C. Green, R.M. Plecenik, E.E. Simonyi, R. Serino: AIP Conference Proceedings No.73, (Carefree, Arizona 1981) pp. 6-9
10. K. Ogawa, I. Shimizu, E. Inoue: Jap. J. Appl. Phys. 20, L639-L642 (1981)
11. R.W. Griffith: Solar Materials Science, chapter 19, (Academic Press 1980), 665-731
12. A. Matsuda, K. Tanaka: Thin Solid Films (1982) in press
13. W.E. Spear, P.G. LeComber: J. Non-Crystalline Solids 8-10, 727-738 (1972)
14. A. Madan, P.G. LeComber, W.E. Spear: J. Non-Crystalline Solids 20, 239-257 (1976)
15. W.E. Spear: Amorphous and Liquid Semiconductors, ed. by J. Stuke and W. Brenig, (Taylor & Francis Ltd. 1974), pp. 1-16
16. A. Madan, P.G. LeComber: Amorphous and Liquid Semiconductors, ed. by W.E. Spear, (CICL, University of Edinburgh, 1977) pp.377-381

17. P.G. LeComber: Fundamental Physics of Amorphous Semiconductors, ed. by F. Yonezawa, Springer Series in Solid-State Sciences 25, pp. 46-55 (1981)
18. W. Paul, A.J. Lewis, G.A.N. Connell, T.D. Moustakas: S.S. Comm. 20, 969-972 (1976).
19. N.B. Goodman, H. Fritzsche: Phil. Mag. B42, 149-165 (1980)
20. M.J. Powell: Phil. Mag. B43, 93-103 (1981)
21. M. Grünewald, P. Thomas, D. Würtz: Phys. Stat. Sol.(b) 100, K139-K143 (1980)
22. R.L. Weisfield, D.A. Anderson: Phil. Mag. B44, 83-93 (1981)
23. M. Grünewald, K. Weber, W. Fuhs, P. Thomas: J. de Physique 42,
24. R.J. Loveland, W.E. Spear, A. Al-Sharbaty: J. Non-Crystalline Solids 13, 55-68 (1973-4)
25. W.E. Spear, R.J. Loveland, A. Al-Sharbaty: J. Non-Crystalline Solids 15, 410-422 (1974)
26. W.E. Spear, P.G. LeComber: Solid State Comm. 17, 1193-1196 (1975)
27. W.E. Spear, P.G. LeComber: Phil. Mag. 33, 935-949 (1976)
28. G. Müller, S. Kalbitzer, W.E. Spear, P.G. LeComber: Amorphous and Liquid Semiconductors, ed. by W.E. Spear, (CICL, University of Edinburgh, 1977) pp. 442-446
29. S. Kalbitzer, G. Müller, P.G. LeComber, W.E. Spear: Phil. Mag. B41, 439-456 (1980)
30. J.D. Cohen, D.V. Lang, J.C. Bean, J.P. Harbison: Phys. Rev. Letters 45, 197-200 (1980)
31. J.D. Cohen, D.V. Lang, J.C. Bean, J. Harbison: J. Non-Crystalline Solids 35/36, 581-586 (1980)
32. D.V. Lang, J.D. Cohen, J.P. Harbison: Phys. Rev. B, at press (1982)
33. W. den Boer: J. de Physique 42, C4, 451-454 (1981)
34. K.D. Mackenzie, W.E. Spear, P.G. LeComber: Phil Mag. (1982) at press.

35. D.A. Anderson and W.E. Spear: Phil. Mag. 36, 695-712 (1977)

36. D. Allan: Phil. Mag. B38, 381-392 (1978)

37. D. Allan, P.G. LeComber, W.E. Spear: Proc. 7th International Conf. on Amorphous and Liquid Semiconductors (ed. W.E. Spear), Edinburgh, 1977

38. P.G. LeComber and W.E. Spear: Topics in Applied Physics Vol.36 (ed. M.H. Brodsky) Springer Verlag, 1979

39. W. Beyer, A. Medeišis, H. Mell: Commun. Phys. 2, 121 (1977)

40. D.I. Jones, P.G. LeComber and W.E. Spear: Phil. Mag. 36, 541-551 (1977)

41. H. Overhof and W. Beyer: Phil. Mag. B43, 433 (1981)

42. L. Friedman: J. Non-Crystalline Solids 6, 329-341 (1971)

43. D. Emin: Phil. Mag. 35, 1189-1198 (1977)

44. P.G. LeComber, D.I. Jones, W.E. Spear: Phil. Mag. 35, 1173-1187 (1977)

45. T.P. Brody, J.A. Asars, G.D. Dixon: IEEE Trans. ED-20, 995-1001 (1973)

46. P.G. LeComber, W.E. Spear, A. Ghaith: Electron Lett. 15, 179-180 (1979)

47. P.G. LeComber, A.J. Snell, K.D. Mackenzie, W.E. Spear: J. de Physique 42, C4, 423-432 (1981)

48. A.J. Snell, K.D. Mackenzie, W.E. Spear, P.G. LeComber, A.J. Hughes: Appl. Phys. 24, 357-362 (1981)

49. I. French, A.J. Snell, P.G. LeComber, J. Stephens: to be published

50. M. Matsumura, H. Hayama: Proc. IEEE 68, 1349-1350 (1980)

51. M. Matsumura, H. Hayama, Y. Nara, K. Ishibashi: IEEE-EDL-1, 182-184 (1980)

52. A.J. Snell, W.E. Spear, P.G. LeComber, K.D. Mackenzie: Appl. Phys. A26, 83-86 (1981)

53. P.K. Weimer, W.S. Pike, G. Sadasiv, F.V. Shallcross, L. Meray-Hovarth: IEEE Spectrum 6, 52-65 (1969)

54. W.E. Spear, P.G. LeComber, S. Kinmond, M.H. Brodsky: Appl. Phys. Letters 28, 105-107 (1976)

55. R.H. Williams, R.R. Varma, W.E. Spear, P.G. LeComber: J. Phys. C12, L209-L213 (1979)

56. W.E. Spear, P.G. LeComber, S. Kalbitzer, G. Müller: Phil. Mag. B39, 159-165 (1979)

57. W. Beyer, R. Fischer: Appl. Phys. Letters 31, 850 (1978)

58. W.E. Spear, R.A. Gibson, D. Yang, P.G. LeComber, G. Müller, S. Kalbitzer: J. de Physique 42, C4, 1143-1153 (1981)

59. G. Müller, P.G. LeComber: Phil. Mag. B43, 419-431 (1981)

60. W.E. Spear, P.G. LeComber, A.J. Snell: Phil. Mag. B38, 303-317 (1978)

61. A.J. Snell, K.D. Mackenzie, P.G. LeComber, W.E. Spear: Phil. Mag. B40, 1-15 (1979)

62. J. Beichler, W. Fuhs, M. Mell, H.M. Welsch: J. Non-Crystalline Solids 35/36, 587-592 (1980)

63. A.J. Snell, W.E. Spear, P.G. LeComber: Phil. Mag. B43 407-417 (1981)

64. A.J. Snell, W.E. Spear, P.G. LeComber: J. Phys. Soc. Japan 49, Suppl.A, 1217-1220 (1980)

65. R.A. Gibson, P.G. LeComber, W.E. Spear: Appl. Phys. 21, 307-311 (1980)

66. D.E. Carlson, C.R. Wronski: Appl. Phys. Letters 29, 602-605 (1976)

67. D.L. Staebler: J. Non-Crystalline Solids 35/36, 387-390 (1980)

68. A.R. Moore: Appl. Phys. Letters 37, 327-330 (1980)

69. J. Dresner, D.J. Szostak, B. Goldstein: AIP Conference Proceedings No.73 (Carefree, Arizona 1981) p.317

70. R. Abeles, C.R. Wronski, Y. Goldstein, H.E. Stasiewski, D. Gutkowicz-Krusin, T. Tiedje, G.D. Cody: AIP Conference Proceedings No.73 (Carefree Arizona 1981) pp. 298-301

71. K. Hecht: Z. Phys. 77, 235-245 (1932)

72. L. Onsager: Phys. Rev. 54, 554-557 (1938)

73. D.M. Pai, R.C. Enck: Phys. Rev. B11, 5163-5174 (1975)

74. R.R. Chance, C.L. Braun: J. Chem. Phys. 59, 2269-2272 (1973)

75. J. Mort, A. Troup, M. Morgan, S. Grammatica, J.C. Knights, R. Lujan: Appl. Phys. Letters 38, 277-279 (1981)

76. J. Mort, I. Chen, A. Troup, M. Morgan, J.C. Knights, R. Lujan: Phys. Rev. Letters 45, 1348-1351 (1980)

77. J. Mort, S. Grammatica, J.C. Knights, R. Lujan: Solar Cells 2, 451 (1980)

78. I. Chen, J. Mort: Appl. Phys. Letters 37, 952-955 (1981)

79. M. Silver, A. Madan, D. Adler, W. Czubatyj: Paper presented at the 14th IEEE Photovoltaic Conference, San Diego, (1980)

80. Y. Hamakawa: J. de Physique 42,C4, 1131-1142 (1981)

81. W.E. Spear, F. Carasco, P.G. LeComber: (in press)

82. I. Shimizu, S. Oda, K. Saito, H. Tomita, E. Inoue: J. de Physique 42, C4, 1123-1130 (1981)

83. ibid. AIP Conference No. 73 (Carefree, Arizona 1981) pp. 288-292

84. I. Shimizu, T. Komatsu, K. Saito, E. Inoue: J. Non-Crystalline Solids 35/36, 773-778 (1980)

85. A.E. Owen, P.G. LeComber, G. Sarrabayrouse, W.E. Spear: IEE (in press)

86. S. R. Ovshinski: Phys. Rev. Letters 21, 1450-1453 (1968)

87. A.E. Owen, J.M. Robertson, IEEE Trans. ED., ED-20, 105-122 (1973)

88. S. Vepřek, V. Maraček: Solid State Electronics 11, 683-684 (1968)

89. A.P. Webb, S. Vepřek: Chem. Phys. Letters 62, 173-177 (1979)

90. S. Vepřek: Chimia 34, 489-501 (1980)

91. S. Vepřek, Z. Iqbal, H.R. Oswald, A.P. Webb: J. Phys. C 14, 295-308 (1981)

92. S.Usui, M. Kikuchi: J. Non-Crystalline Solids 34, 1-11 (1979)

93. A. Matsuda, S.Yamasaki, K. Nakagawa, H. Okushi, K. Tanaka, S. Iizima, M. Matsumara, H. Yamamoto: Jap. J. of Appl. Phys. 19, L305-L308 (1980)

94. T. Hamasaki, H. Kurata, M.Hirose, Y. Osaka: Appl. Phys. Letters 37, 1084-1086 (1980)

95. W.E. Spear, G. Willeke, P.G. LeComber, A.G. Fitzgerald: J. de Physique 42, C4, 257-260 (1981)

96. A. Matsuda, H. Matsumura, S. Yamasaki, H. Yamamoto, T. Imura, H. Okushi, S. Iizima, K. Tanaka: Jap. J. of Appl. Phys. 20, L183-L186 (1981)

97. T. Hamasaki, H. Kurata, M. Hirose, Y. Osaka: Jap. J. of Appl. Phys. 20, L84-L86 (1981)

98. A. Madan, S.R. Ovshinsky, E. Benn: Phil. Mag. 40, 259-277 (1979)

99. O. Reilly, W.E. Spear: Phil. Mag. B38, 295-302 (1978)

100. G. Willeke, W.E. Spear, D.I. Jones, P.G. LeComber: Phil.Mag. (1982) in press

101. G.L. Pearson, J. Bardeen: Phys. Rev. 75, 865-883 (1949)

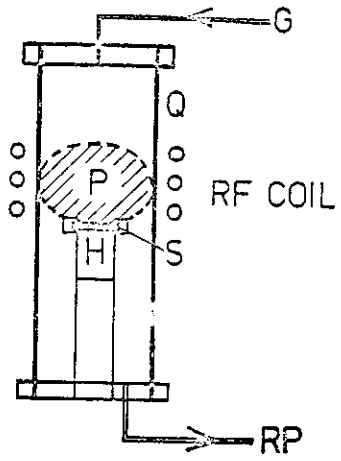

Fig.1 Inductively coupled glow discharge deposition system. G, gas; Q, fused silica reaction tube; S, substrate, H, heated pedestal; RP, rotary pump; P, plasma.

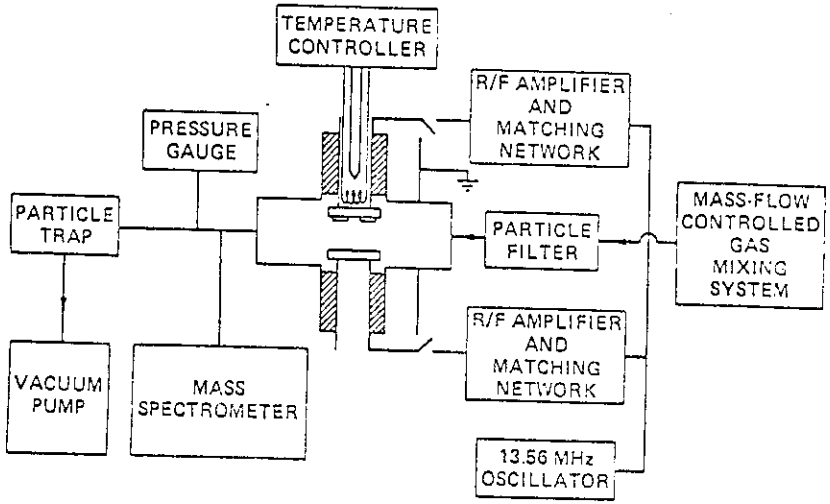

Fig.2 Capacitatively coupled glow discharge deposition system designed by Knights [5][6].

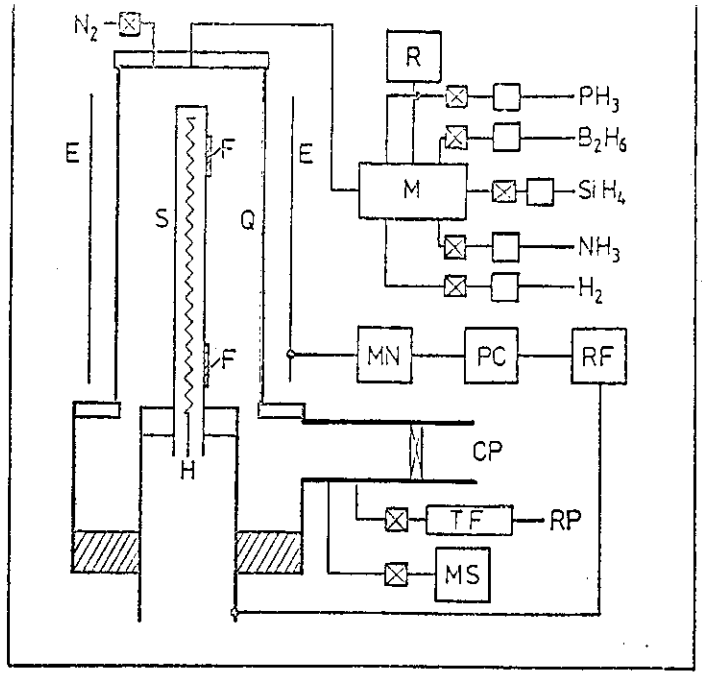

Fig.3 Vertical glow discharge deposition system used at the Dundee laboratory. S, specimen holder; H, electrically insulated heater; Q, quartz enclosure; E, external r.f. electrodes; F, rotatable 'flaps' for shading during run; M, mixing chamber; R, reservoir for pre-mixing of gases; MN, matching network; PC, power controller; RF, r.f. generator; CP, cryo-pump; TF, tubular furnace; RP, rotary pump; MS, mass spectrometer.

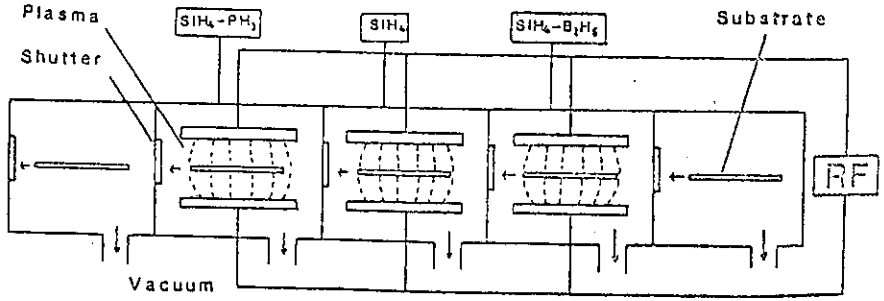

Fig.4 Industrial glow discharge reactor designed by the Sanyo laboratories [7].

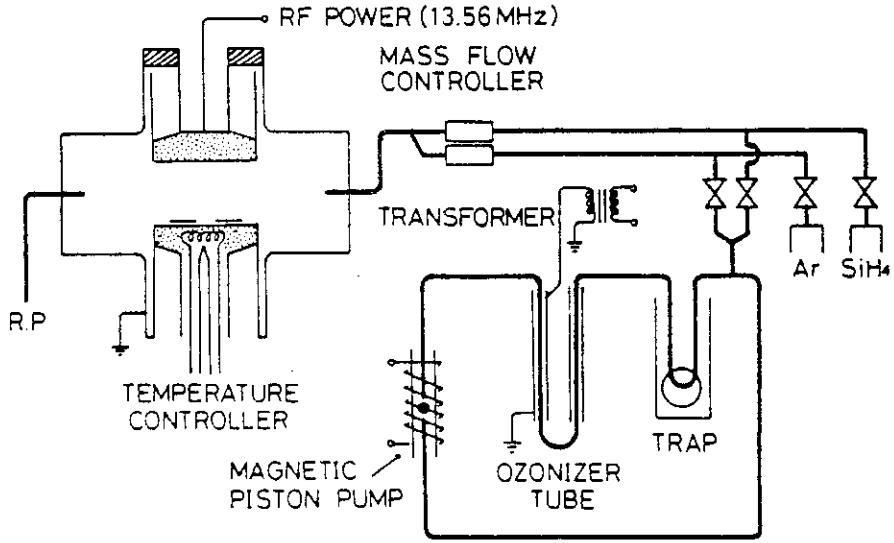

Fig.5 Glow discharge deposition unit showing method of producing higher silanes. After ref. 10

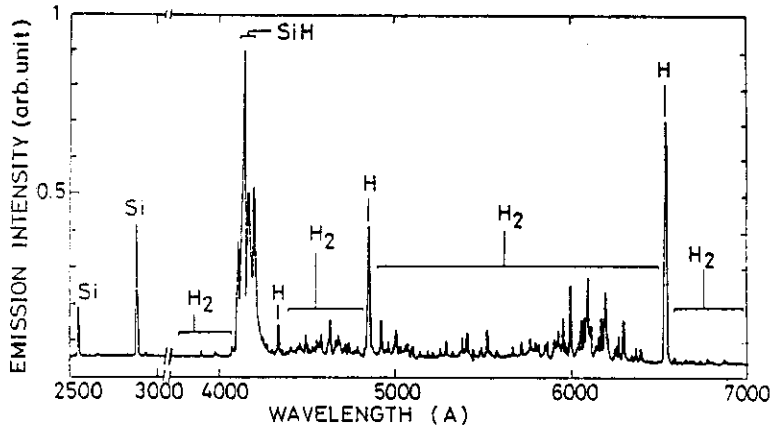

Fig.6 Optical emission spectrum from a pure silane glow discharge plasma run at a power of 20W. After ref. 12.

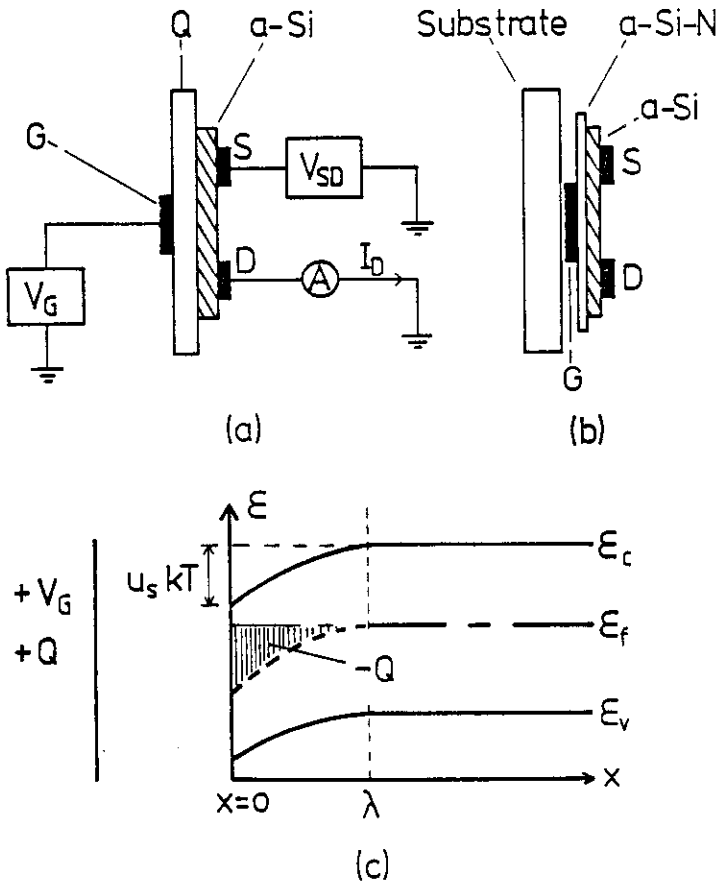

Fig.7 (a) and (b) specimen geometries used in the field effect experiments. S, D and G represent the source, drain and gate electrodes. Q is the thin quartz dielectric. (c) electron energy ϵ plotted as a function of distance from the a-Si/dielectric interface at x = o. $u_s kT$ denotes the magnitude of the band bending at the interface and λ its spatial extent into the semiconductor. Q and -Q represent the total charge induced on the gate and in the a-Si respectively by the positive gate voltage V_G.

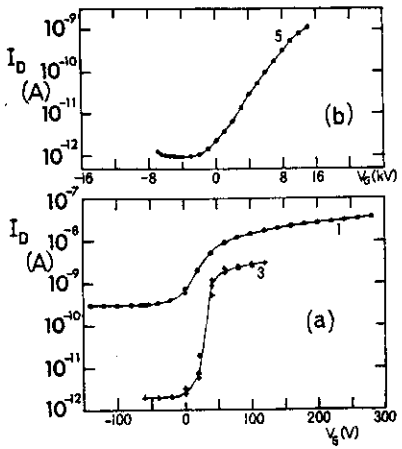

Fig.8 The dependence of the specimen source-drain current I_D on the gate potential V_G for a number of glow discharge specimens deposited at about 250°C. (a) Si-N dielectri and (b) quartz dielectric. After ref.14.

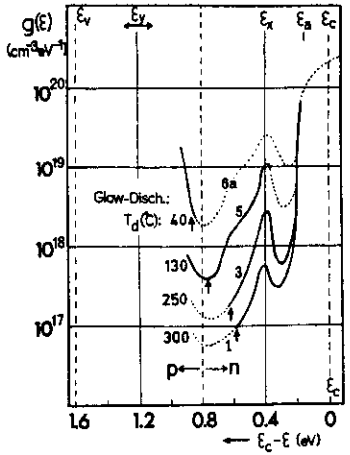

Fig.10 Deduced density of states for glow discharge specimens deposited at the given temperatures T_d. The position of the Fermi level is indicated by the arrow. Full lines were calculated from experimental data and the dotted parts were based on an extrapolation procedure. After ref. 14.

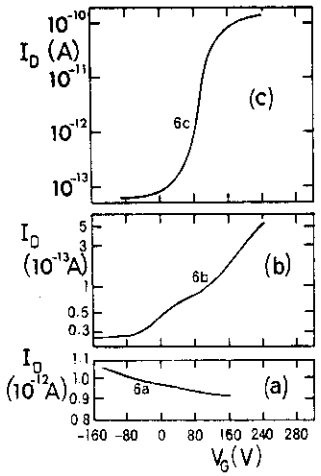

Fig.9 Field effect results for a specimen deposited at a low deposition temperature (T_d = 40°C). (a) as deposited, (b) annealed to 140°C and (c) annealed to 210°C. After ref.14.

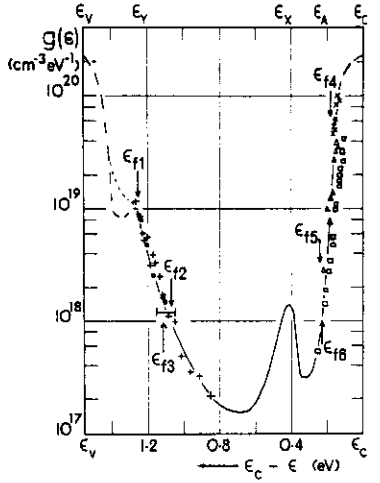

Fig.11 Density of states of high T_d glow discharge samples. The centre region refers to undoped specimens and the points to comparatively lightly doped specimens: ε_{f6}, ε_{f5} and ε_{f4}, Fermi level positions of P-doped samples; ε_{f3}, ε_{f2} and ε_{f1}, Fermi level positions of B-doped samples.

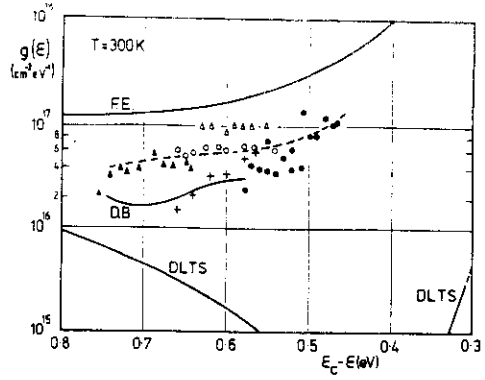

Fig.12 Density of states in glow discharge a-Si deduced from different experiments: F.E., field effect (after ref.14 and 16); solid line D.B., space charge limited currents (after ref.33); dashed line and experimental points, space charge limited currents (after ref.34); DLTS, deep level transient spectroscopy (after ref.32).

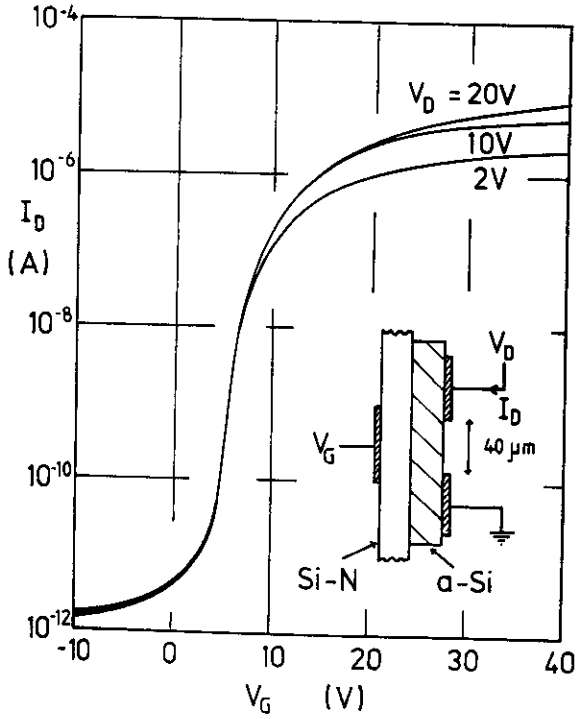

Fig.13 Transfer characteristics of a-Si FET element. The drain current I_D is plotted against the gate voltage V_G for three drain potentials V_D. The insert shows the basic design of the FET. After ref.48

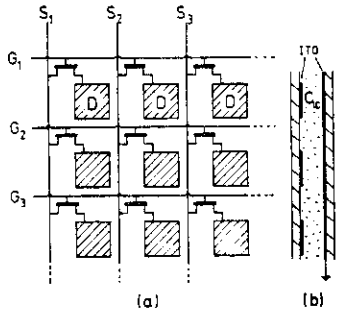

Fig.14 Schematic lay-out of an addressable liquid crystal panel. (a) shows gate and source connections G_1,G_2 ... and S_1,S_2 ..., and the drain connected to the ITO squares D. (b) section through panel. C_{LC} denotes the capacitance of a liquid crystal element. After ref.48.

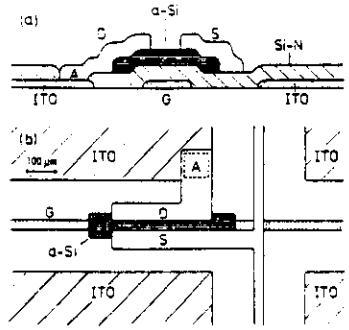

Fig.15 Design of a-Si field effect transistor element. (a) section through device, (b) FET in part of the matrix array (ITO: indium-tin oxide squares; G: gate electrode; D: drain electrode; S: source electrode; A: contact hole etched through silicon nitride film). After ref.48.

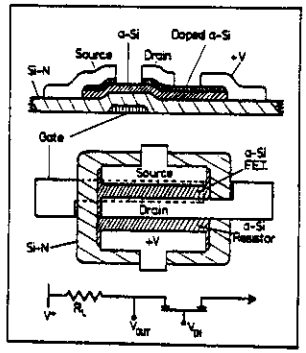

(a)

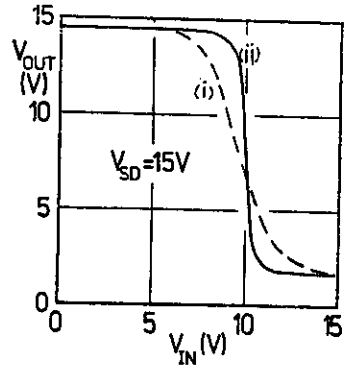

(b)

Fig.16 (a) Section and plan view of the integrated a-Si inverter. After ref.52

(b) Characteristics of (i) single a-Si inverter and (ii) three inverters connected in series. After refs 52, 47.

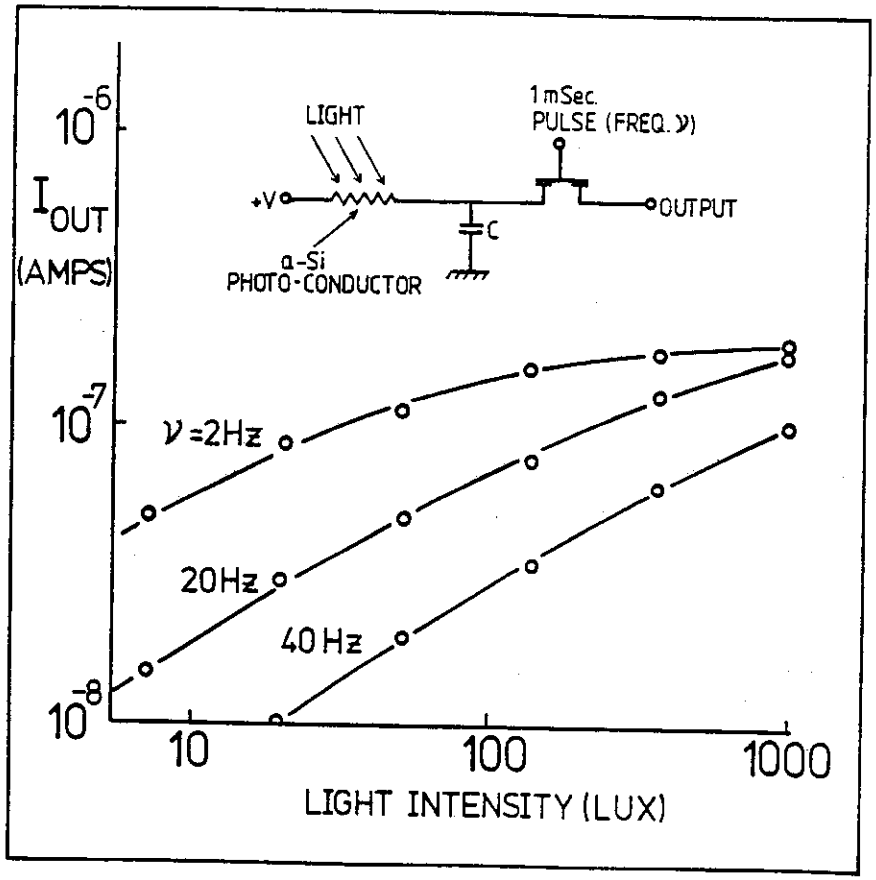

Fig.17 Circuit of the a-Si image sensor and measured output current as a function of light intensity for various gate pulse frequencies. After refs. 47,52.

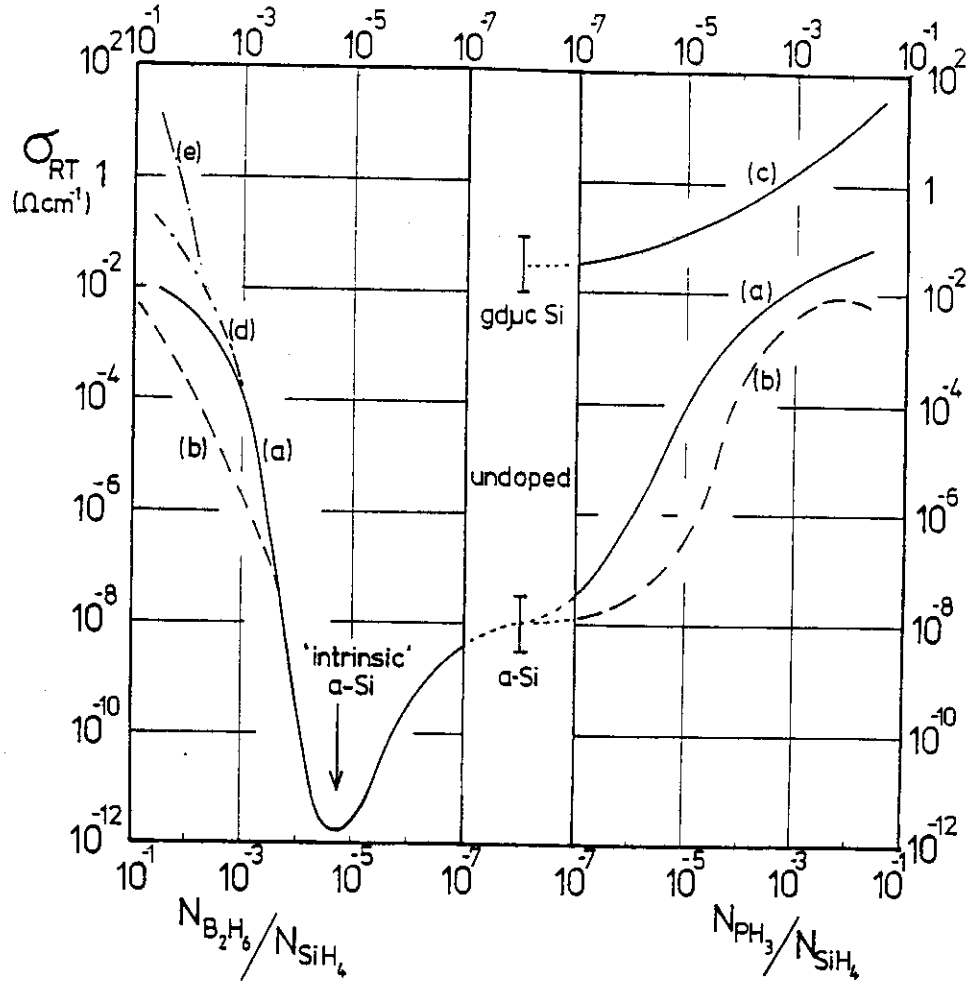

Fig.18. Doping dependence of the room temperature conductivity σ_{RT} of glow discharge Si. On the right σ_{RT} is plotted against the phosphine doping ratio, on the left against the diborane doping ratio. The centre refers to the undoped material. Curve (a) refers to specimens prepared in the system shown in Fig.3, curve (b) to the doping results published originally in 1976 [27]. Curves (c), (d) and (e) were obtained from micro-crystalline Si specimens prepared in the glow discharge (see Section 8.2).

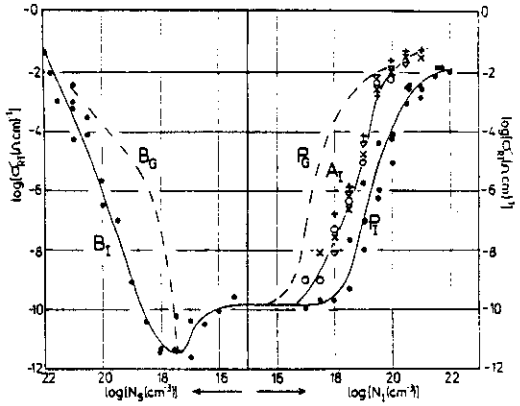

Fig.19 Doping of a-Si by ion implantation. The room temperature conductivity σ_{RT} is plotted against the impurity concentration. P_I, phosphorus ion implantation; A_I, alkali ion implantations (oNa, + K, ▽Rb, xCs); B_I, boron ion implantations. All implantations at a specimen temperature of 280°C. P_G, B_G represent the results for gas phase doping. After ref.29.

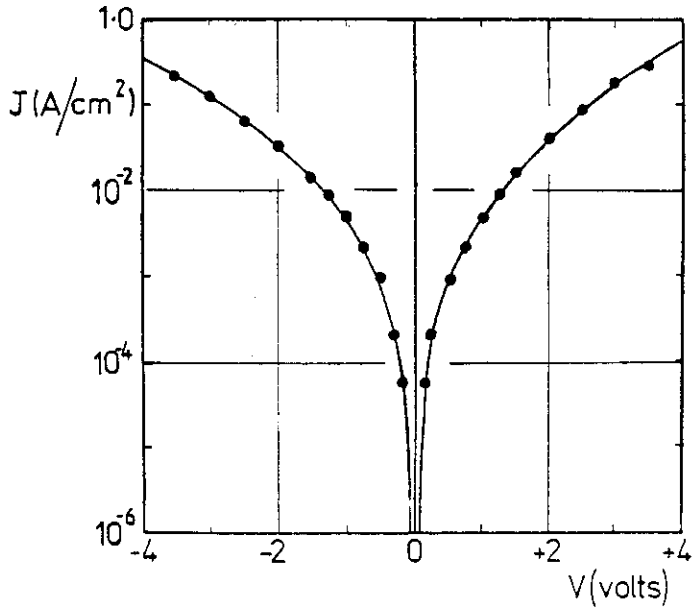

Fig.20 Current density J plotted against the applied voltage V for a symmetric n^+-i-n^+ structure. The graph illustrates the remarkable injecting properties of the n^+-contact. After ref. 34.

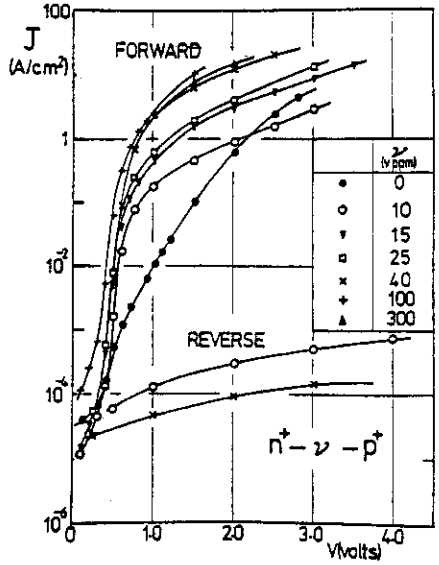

Fig.21 Forward and reverse current density/applied voltage characteristics for n^+-ν-p^+ diodes showing the effect of different gaseous doping ratios (in vppm) on the central ν-region. After ref.65

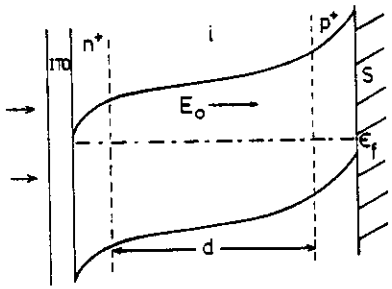

Fig.22 Electron energy profile through an a-Si p^+-i-n^+ photovoltaic junction. S, stainless steel substrate; E_o, built-in electric field; ITO, transparent electrode.

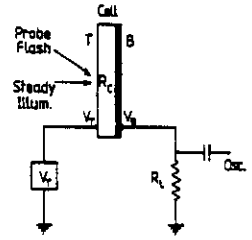

Fig.23 Basic circuit used in the transient experiments. After ref.58

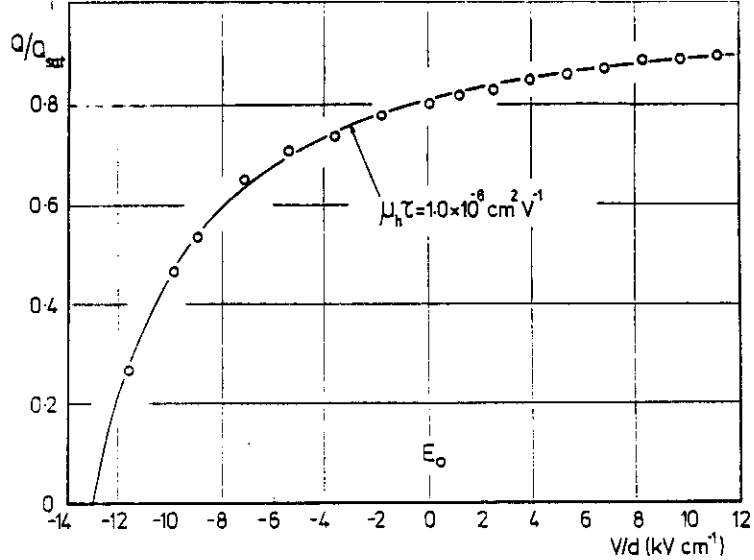

Fig.24 Results of transient integrated pulse height measurements. The computer fit to Eqn.(7) gives the $\mu_h\tau$ value of 1.0×10^{-8} cm^2V^{-1}. After ref. 58

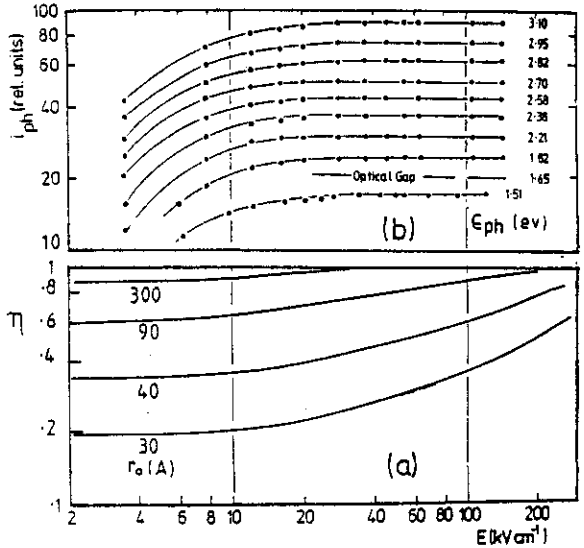

Fig.25 (a) field dependence of the generation efficiency η calculated from the Onsager theory [72] for the thermalisation lengths r_o given on the diagram.

(b) observed field dependence of the short-circuit photocurrent in a p^+-i-n^+ junction. i_{ph} is plotted in arbitrary units and the curves have been separated to show the absence of any field dependence above about 20kV cm^{-1}. After ref. 81.

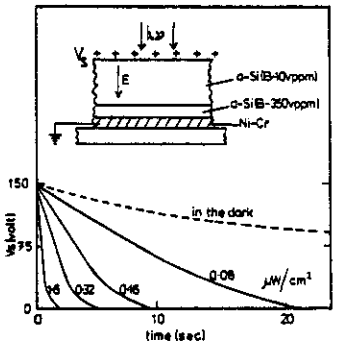

Fig.26 a-Si photoreceptor for electrophotography. The diagram shows the structure of the layer and the time dependence of the surface potential V_S in the dark and at the light levels indicated. After ref. 82

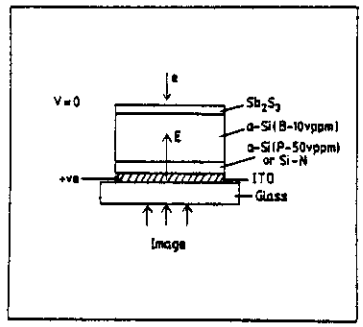

Fig.27 Structure of an a-Si Vidicon target. After ref. 82

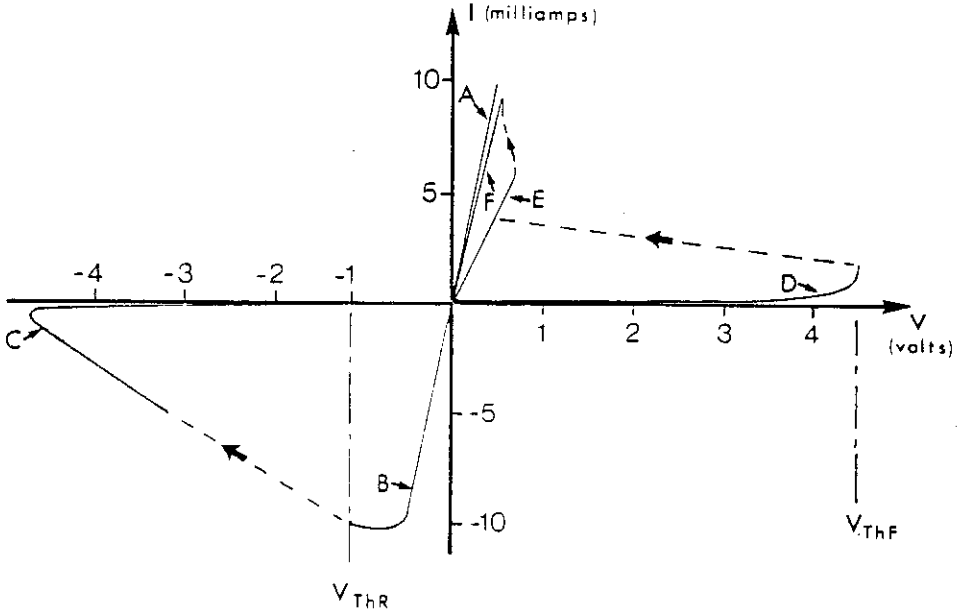

Fig.28 D.C. characteristics of a non-volatile, programmable a-Si memory device. V_{THF} and V_{THR} are the forward and reverse threshold voltages for switching the device into the on- and off-state respectively. After ref. 85

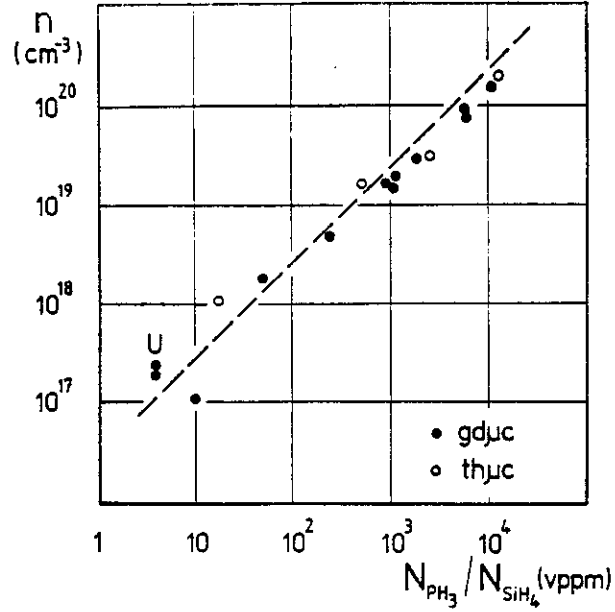

Fig.29 Electron density n from room temperature Hall effect measurements plotted against the gaseous doping ratio for gdμc Si and thermally crystallised specimens. After ref. 95

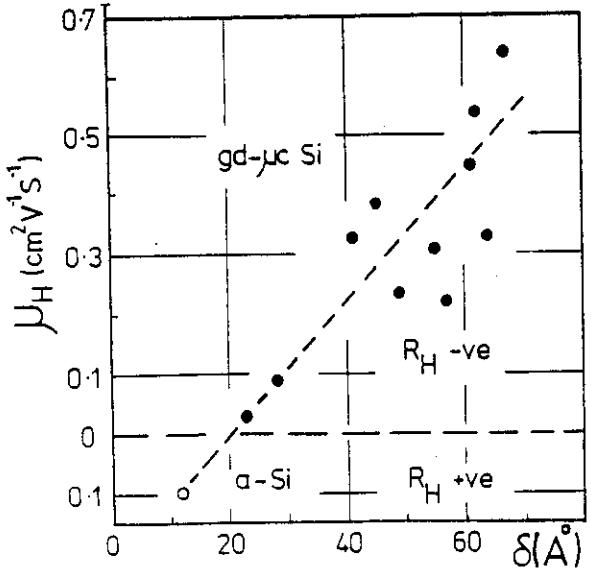

Fig.30 Hall mobility in gdμc Si specimens plotted against the crystallite size δ. The open circle denotes a typical result for a-Si, showing an anomalous sign of the Hall constant R_H. After ref. 95

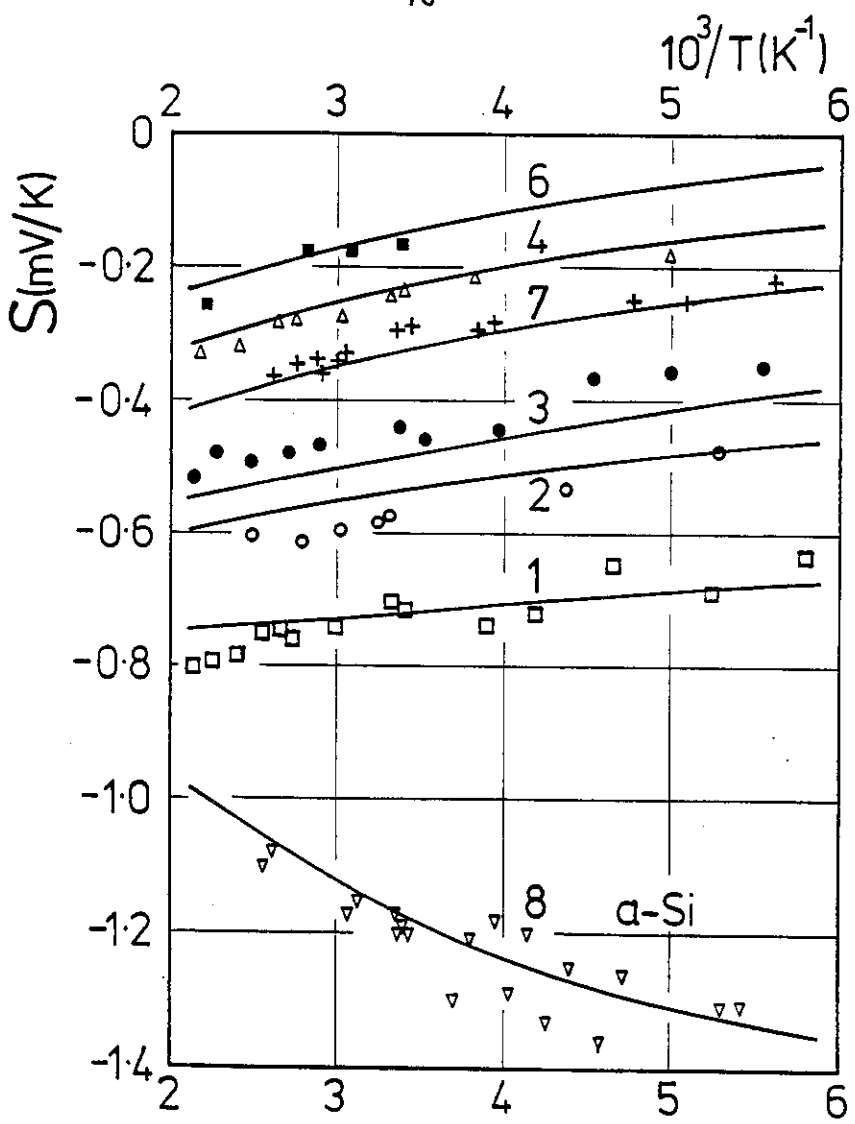

Fig.31 Temperature dependence of the thermoelectric power. Experimental points 1-6: gduc specimens with increasing phosphorus doping; 7: thermally crystallised specimen; 8: a-Si specimen. Solid lines are calculated curves. After ref. 100

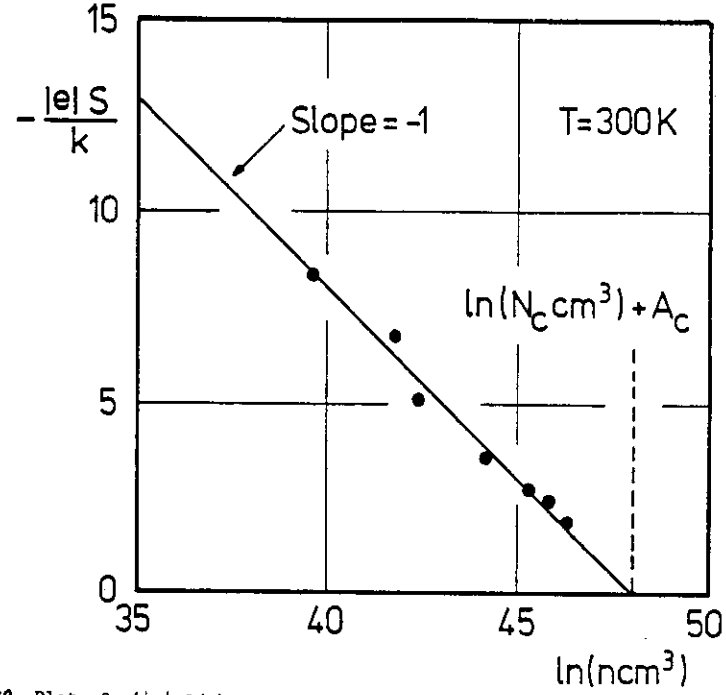

Fig.32 Plot of $-(|e|\ S/k)$ against ln n at T = 300K as a test of Eqn. After ref. 100

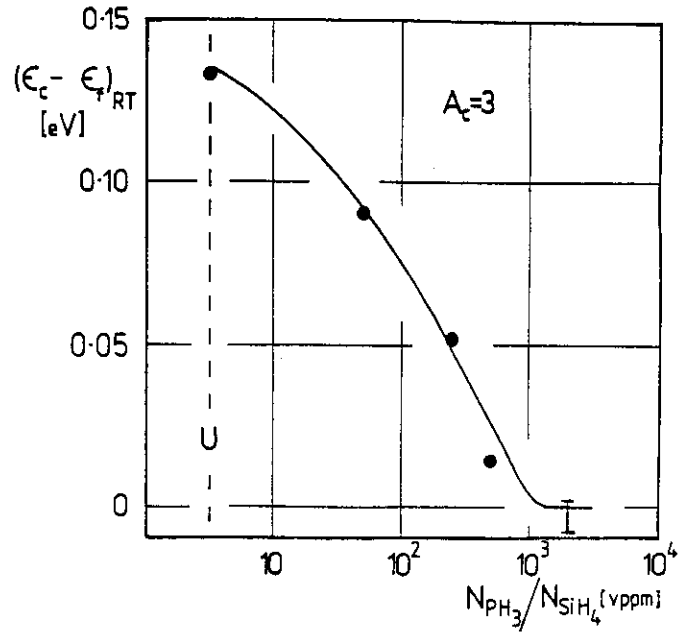

Fig.33 The room temperature value of $\epsilon_c - \epsilon_f$ plotted against the gaseous doping ratio for Ac = 3. After ref. 100